12-14-2015

# Wavelet Analysis of Periodic Error in Heterodyne Interferometry

Chao Lu
*University of South Carolina - Columbia*

# WAVELET ANALYSIS OF PERIODIC ERROR IN HETERODYNE INTERFEROMETRY

by

Chao Lu

Bachelor of Science
Tsinghua University, 2012

---

Submitted in Partial Fulfillment of the Requirements

For the Degree of Master of Science in

Mechanical Engineering

College of Engineering and Computing

University of South Carolina

2015

Accepted by:

Joshua A. Tarbutton, Director of Thesis

Lingyu Yu, Reader

Lacy Ford, Senior Vice Provost and Dean of Graduate Studies

# DEDICATION

This work is dedicated to my parents, whose love and support make the impossible possible.

## ACKNOWLEDGEMENTS

I would like to express my deepest gratitude to my advisor, Dr. Joshua Tarbutton, for his guidance, encouragement and patience. I also wish to express my thanks to the thesis reader, Dr. Lingyu Yu.

## ABSTRACT

Heterodyne displacement measuring interferometry provides important metrology for applications requiring high resolution and accuracy. Heterodyne Michelson interferometers use a two-frequency laser source and separate the two optical frequencies into one fixed length and one variable length path via polarization. Ideally these two beams are linearly polarized and orthogonal so that only one frequency is directed toward each path. An interference signal is obtained by recombining the light from the two paths; this results in a measurement signal at the heterodyne (split) frequency of the laser source. This measurement signal is compared to the optical reference signal. Motion in the measurement arm causes a Doppler shift of the heterodyne frequency which is measured as a continuous phase shift that is proportional to displacement. In practice, due to component imperfections, undesirable frequency mixing occurs which yields periodic errors. Ultimately, this error can limit the accuracy to approximately the nanometer level. Periodic error is typically quantified using a Fourier transform-based analysis of constant velocity motions. However, non-constant velocity profiles lead to non-stationary signals that require alternate analysis techniques for real-time compensation.

The objective of this study is to design a new discrete time continuous wavelet transform (DTCWT)-based algorithm, which can be implemented in real time to quantify and compensate periodic error for constant and non-constant velocity motion in heterodyne interferometer. It identifies the periodic error by measuring the phase and amplitude information at different orders (the periodic error is modeled as a summation

of pure sine signals), reconstructs the periodic error by combining the magnitudes for all orders, and compensates the periodic error by subtracting the reconstructed error from the displacement signal measured by the interferometer. The algorithm is validated by comparing the compensated results with a traditional frequency domain approach for constant velocity motion. For a linear displacement signal where first and second order periodic errors (amplitudes 4 nm and 2.5 nm, respectively) are superimposed during a constant velocity (50 mm/min) displacement, the wavelet-based algorithm demonstrates successful reduction of the first order periodic error amplitude to 0.24 nm (a 94% decrease) and a reduction of the second order periodic error to 0.3 nm (an 88% decrease).

# TABLE OF CONTENTS

# LIST OF FIGURES

# LIST OF SYMBOLS

| | |
|---|---|
| $E$ | Light wave amplitude. |
| $f$ | Light wave frequency. |
| $\lambda$ | Light wave wavelength. |
| $\phi$ | Phase. |
| $\omega$ | Angular frequency. |
| $T$ | Temperature. |
| $P$ | Pressure. |
| $H$ | Humidity. |
| $\varphi$ | Scaling function. |
| $\psi$ | Wavelet function. |
| $u$ | Shift parameter in the continuous wavelet transform. |
| $s$ | Scale parameter in the continuous wavelet transform. |
| $W$ | The continuous wavelet transform operation. |
| $A$ | Periodic error amplitude. |

## List of Abbreviations

CWT ..... Continuous Wavelet Transform

DTCWT ..... Discrete Time Continuous Wavelet Transform

DWT ..... Discrete Wavelet Transform

HWP ..... Half Wave Plate

LP ..... Linear Polarizer

PBS ..... Polarizing Beam Splitter

RMS ..... Root Mean Square

RR ..... Retroreflector

WT ..... Wavelet Transform

# CHAPTER 1

## INTRODUCTION

Since first introduced in the early 1960s, the displacement measuring interferometer has provided high accuracy, long range and high resolution for dimensional metrology. The interferometer is used in a number of non-contact displacement measurement applications including: 1) position feedback of lithographic stages for semiconductor fabrication; 2) transducer calibration; and 3) position feedback/calibration for other metrology systems. In these situations, Heterodyne (two-frequency) Michelson-type interferometers with single, double, or multiple passes of optical paths is a common configuration choice. These systems infer changes in the selected optical path length difference by monitoring the optically induced variation in the photodetector, where current is generated proportional to the optical interference signal. The current is processed and converted to voltage and the phase is determined by phase-measuring electronics. The measured phase change is nominally linearly proportional to the displacement of the measurement target, based on ideal performance of the optic elements.

There are many well-known error sources that can degrade the accuracy of the system [1-5]. These include cosine error, Abbe error, refractive index uncertainty, thermal drift and deadpath. These errors can be compensated by setup changes or additional metrology approaches. Other errors, such as electronics error and source vacuum wavelength uncertainty, are usually small. Frequency mixing in heterodyne

interferometer resulting from non-ideal performance of the optical system causes periodic errors which are superimposed on the measured displacement signal. For heterodyne interferometers, both first and second order periodic errors occur, which correspond to one and two periods per displacement fringe. Periodic error is an intrinsic error in the heterodyne interferometer that can limit the accuracy to the nanometer level (or higher) depending on the optical setup. This is true when the interferometer is operated in vacuum to minimize the error associated with refractive index uncertainty due to uncompensated fluctuations in temperature, pressure, and humidity. While any of these error sources may dominate in a given situation, the focus of this study is periodic error.

To compensate this error, real-time digital error measurement may be applied, as it requires no change to the optical system, which allows convenient implementation for existing systems. Previous research has demonstrated a frequency domain approach to periodic error identification [6-8], where the periodic error is measured by calculating the Fourier transform of the time domain data collected during constant velocity target motion. The periodic errors are then determined from the relative amplitudes of the peaks in the frequency spectrum. For an accelerating or decelerating motion, however, the Doppler frequency varies with velocity. In this case, the frequency domain approach is not well-suited because the Fourier transform assumes stationary signals. To overcome this limitation, a wavelet-based analysis is applied here to measure and compensate periodic error.

The wavelet analysis has been widely used as an analytical tool for numerical analysis, mathematical modeling, and signal processing. The transform is computed at various locations of the signal and for various scales of the wavelet, thus filling up the

transform plane. This is done in a smooth continuous fashion for the continuous wavelet transform (CWT). A CWT of a time domain signal provides information in both the temporal and frequency domains [9]. For example, calculating the Morlet CWT enables the frequency content of a signal to be observed at different times. The CWT can be more informative than the Fourier transform because the CWT shows the relationship between frequency content and signal based on the wavelet scale and the time period. This enables the frequency and time information of the signal to be determined simultaneously by applying an appropriate wavelet. When applied to non-stationary signals, the CWT can supply frequency information at any time.

A wavelet-based analysis is a novel approach in the study of periodic error measurement and compensation and enables the analysis of non-constant velocity motions. This research introduces a new wavelet analysis algorithm to measure and compensate periodic error for constant velocity target motions. In the following sections of this chapter, foundations in interferometer, and periodic error and its traditional compensation approaches are introduced. This chapter concludes with outline of this thesis.

## 1.1 BACKGROUND

To use monochromatic light as a standard for displacement measurement was first introduced in 1892. Interferometry was used for the measurement of the standard meter by Albert Michelson and Rene Benoit. A schematic of the Michelson interferometer is shown in Figure 1.1. Beam 1 is from an extended light source, and split by a beam splitter with semi-reflective coating on the surface. Two separated beams travel to and reflect

back from two mirrors, M1 and M2 (M2 can move to generate an optical path difference), and then recombine at the same beam splitter. The interference pattern of the recombined beam is imaged on the screen.

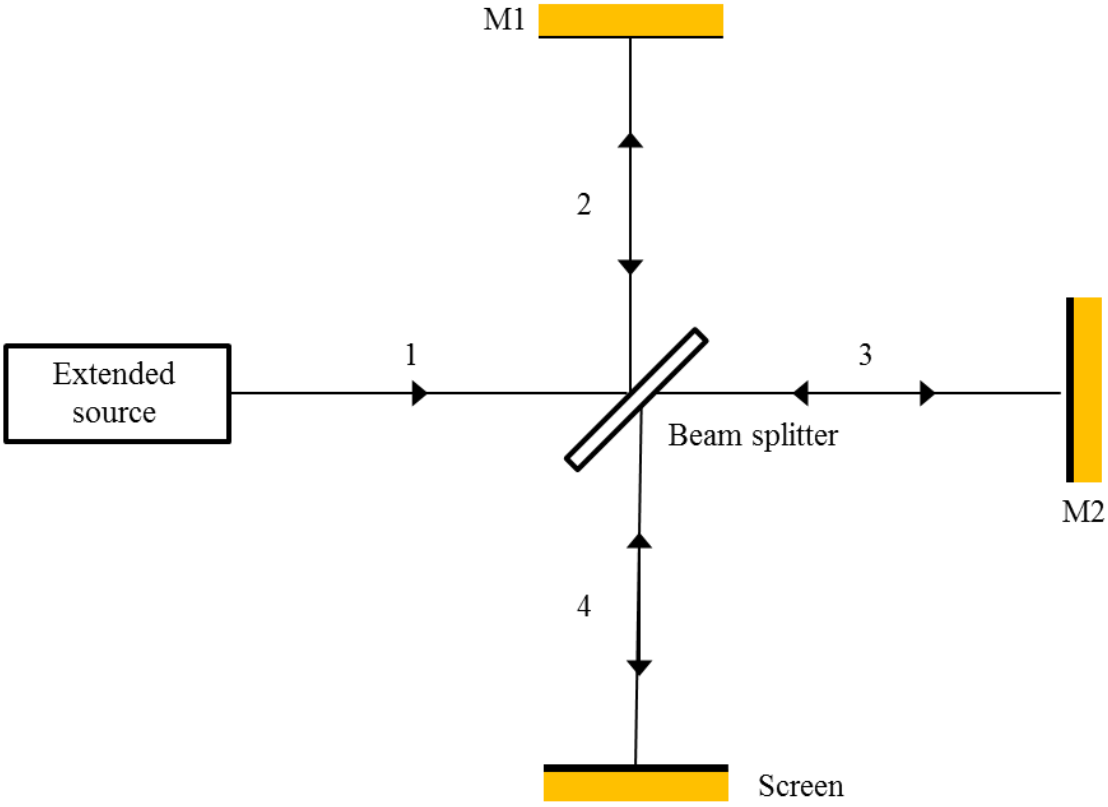


Figure 1.1 Schematic of the Michelson interferometer.

After the development of the He-Ne laser in the 1960s, interferometry has been widely used for precision length and displacement measurement in many demanding applications requiring high resolution and accuracy. In past five decades, the basic configuration of the interferometer, developed by Michelson, remains the same. The modern interferometer has been developed with the improvement in laser source, optics, and signal processing. The extended light source is replaced by the laser, generating monochromatic light, and the screen is replaced by a photodetector, with an added digital

electronics behind to interpret the measurement signal (irradiance variation or phase change) and to convert fringe to displacement.

Currently, polarization encoded heterodyne interferometers have become a standard instrument for displacement measurement. Its difference from a homodyne (single frequency) interferometer is that the laser source in a heterodyne interferometer emits two slightly different frequencies. This difference introduces a number of advantages and results in improved accuracy.

## 1.2 INTERFERENCE

Light can be treated as a transverse electromagnetic wave propagating through space. Usually only the electric field at any point is considered, since the electric and magnetic fields are orthogonal to each other [10].

The electric field can be described as a time-varying vector perpendicular to the direction of propagation of the wave. Due to a light wave propagating along the z direction, the electric field at any point can be expressed as

$$E = E_0 \cos\left[2\pi\left(ft - \frac{z}{\lambda}\right)\right], \tag{1.1}$$

where $E_0$ is the light wave amplitude, $f$ is the frequency, and $\lambda$ is the wavelength. $2\pi(ft - z/\lambda)$ is the phase of the wave, varying with time and location at z-axis. In a vacuum, the light speed is

$$c = f\lambda_v, \tag{1.2}$$

where $\lambda_v$ is the light wavelength in the vacuum. In one medium, the light speed is

$$v = \frac{c}{n}, \tag{1.3}$$

where $n$ is the refractive index of this medium. The light wavelength can be determined by

$$\lambda = \frac{v}{f} = \frac{\frac{f\lambda_v}{n}}{f} = \frac{\lambda_v}{n}. \tag{1.4}$$

Eq. 2.1 can be rewritten as

$$E = E_0 \cos\left[2\pi\left(ft - \frac{nz}{\lambda_v}\right)\right] = E_0 \cos(\omega t - kz), \tag{1.5}$$

where $\omega = 2\pi f$ is the angular frequency, and $k = 2\pi n/\lambda_v$ is the propagation constant.

To be convenient for mathematical operations, complex exponential representation is usually used,

$$E = E_0 e^{-i(\omega t + \phi)}, \tag{1.6}$$

where $\phi = -kz$.

Consider two light waves propagating in the same direction at a given point in space. They are both linearly polarized, and have different amplitudes but the same frequency. They are represented by

$$\begin{aligned} E_1 &= E_{01} e^{-i(\omega t + \phi_1)} \\ E_2 &= E_{02} e^{-i(\omega t + \phi_2)} \end{aligned}, \tag{1.7}$$

where $E_{0i}\,(i = 1, 2)$ are the amplitudes of the light waves, and $\phi_i\,(i = 1, 2)$ is the phase. The Principle of Superposition is that the electric field intensity at one point in space resulting from two or more electromagnetic waves is the vector sum of these electric fields. In fact, the interference is a consequence of this principle. According to the

Principle of Superposition, the resultant electric field, $E$, is given by the addition of the two light waves, $E_1$ and $E_2$,

$$E = E_1 + E_2 = E_{01}e^{-i(\omega t+\phi_1)} + E_{02}e^{-i(\omega t+\phi_2)}, \tag{1.8}$$

The resultant irradiance, $I$, is proportional to the square of the wave amplitude,

$$\begin{aligned} I \propto |E|^2 &= \left|E_{01}e^{-i(\omega t+\phi_1)} + E_{02}e^{-i(\omega t+\phi_2)}\right|^2 \\ &= \left(E_{01}e^{-i(\omega t+\phi_1)} + E_{02}e^{-i(\omega t+\phi_2)}\right)\left(E_{01}^{*}e^{-i(\omega t+\phi_1)} + E_{02}^{*}e^{-i(\omega t+\phi_2)}\right), \\ &= |E_{01}|^2 + |E_{02}|^2 + 2\,\mathrm{Re}\left(E_{01}E_{02}^{*}e^{-i(\phi_1-\phi_2)}\right) \\ &= I_1 + I_2 + 2\sqrt{I_1 I_2}\cos(\phi_1 - \phi_2) \end{aligned} \tag{1.9}$$

where * indicates the complex conjugate, and Re represents the real part of a complex number.

The resultant irradiance shows a periodic characteristic depending on $\phi_1 - \phi_2$. The two light waves constructively interfere when $\cos(\phi_1 - \phi_2)$ reaches its maximum value and the two waves reinforce each other. Destructive interference occurs if $\cos(\phi_1 - \phi_2)$ reaches its minimum and the two waves counteract each other. If the amplitude of the two light waves are equal ($I_1 = I_2 = I_0$), the resultant irradiance is four times the individual irradiance in constructive inference, and attains zero value in destructive inference. The transition from one maximum to the next maximum through a minimum corresponds to a $2\pi$ phase change, which is also an optical path length change of one wave length, referred to as one “fringe”.

## 1.3 TWO DISPLACEMENT MEASURING INTERFEROMETER TYPES

For displacement measurement, two types of the Michelson interferometer are commonly used. One is the homodyne interferometer, which uses a single frequency laser head and converts the intensity variation induced by interferences into displacement. On the other hand, a heterodyne interferometer uses a two-frequency laser source and measures displacement by identifying the phase shift between the reference and measurement signals. Two approaches are introduced in the next two sections.

A Michelson-type interferometer is implemented with a certain configuration (signal, double, or multiple passes of the optical path). The single pass configuration prior to the introduction of two interferometer types will be described. In a single pass configuration (shown in Figure 1.2), a beam with both vertical and horizontal polarization components splits at a polarizing beam splitter (PBS). The horizontally polarized beam is transmitted while the vertically polarized beam is reflected. The transmitted beam (measurement beam) propagates forward to the moving retroreflector and then backward to the polarizing beam; the reflected beam (reference beam) is reflected at the fixed retroreflector. The two measurement and reference beams are recombined at the PBS and brought into interference after passing through a linear polarizer (LP). The phase change of the measurement beam, $\Delta\phi_{single}$, is proportional to double displacement of the moving retroreflector,

$$\Delta\phi_{single} \propto 2d, \tag{1.10}$$

where $d$ is the displacement of the target.

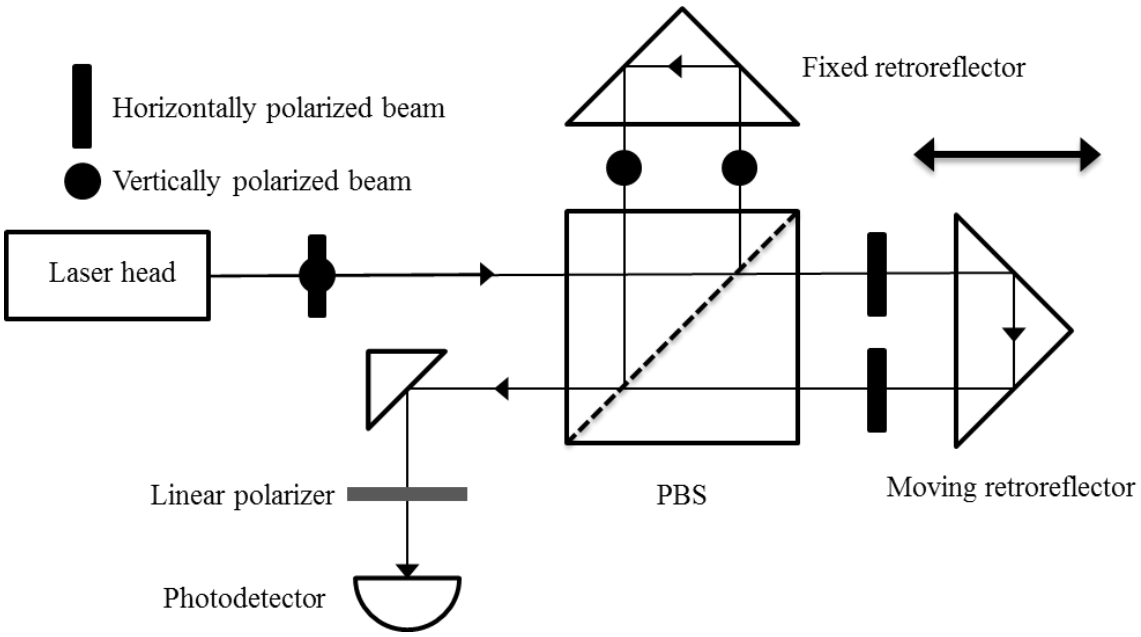


Figure 1.2 Schematic of a single pass interferometer.

The optical resolution of the signal pass system (i.e. the fringe introduced in Section 1.2) is half of the laser wavelength. Thus, in the single pass interferometer, the target displacement can be determined by

$$d = \frac{\lambda}{2} N_{fringe}, \tag{1.11}$$

where $N_{fringe}$ is the number of fringes.

### 1.3.1 HOMODYNE INTERFEROMETER

The basic homodyne interferometer consists of a laser source (single-frequency beam), a polarizing beam splitter, retroreflectors, and a photodetector, as shown in Figure 1.3.

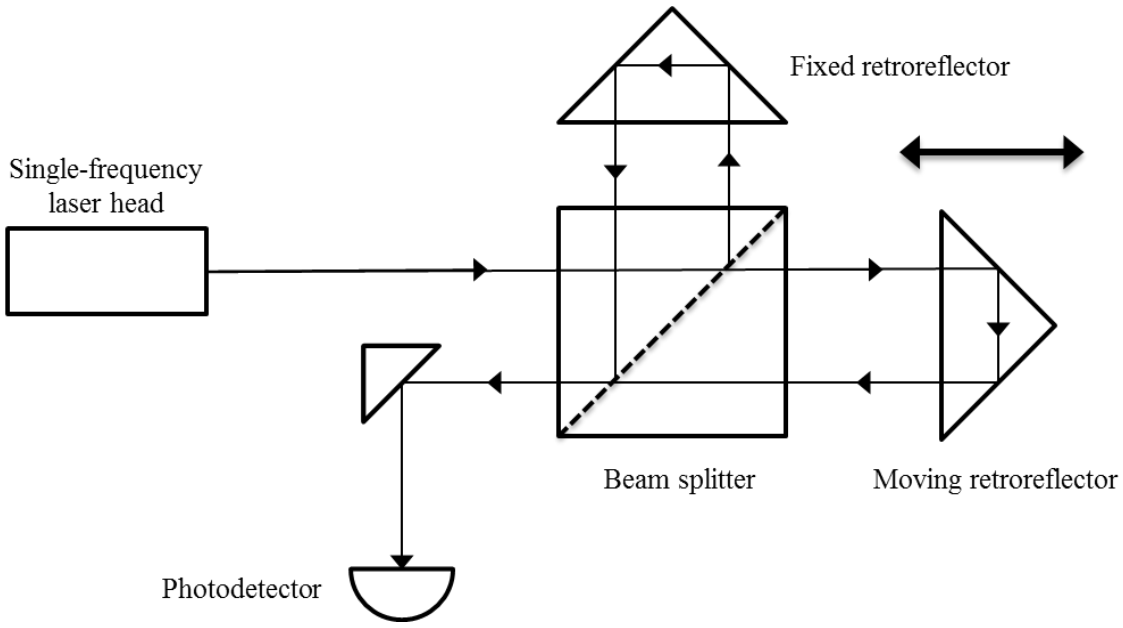


Figure 1.3 Schematic of homodyne interferometer setup.

A single-frequency, linearly polarized beam is typically from a Helium-Neon laser head and oriented at 45 °to the horizontal axis. The beam splitter equally splits this incoming beam into two beams. One beam travels to the fixed retroreflector and reflects back, while another one travels to the moving retroreflector and back. The two beams recombine at the PBS and interfere. The interference signal is finally received at the photodetector. Change in the relative path lengths of the two beams causes a relative phase change in the interference signal. Therefore, the detected irradiance can be expressed in Equation 1.9.

Basic homodyne interferometer advantages:

- System is simple and easy to align.
- It can be used for multi-axis systems.
- Single-point detector used in the system enables faster processing than a CCD array.

Basic homodyne interferometer advantages:

- System is sensitive to laser power fluctuations and stray light.
- System is sensitive to tilting.
- It cannot detect the direction sense of the target.

### 1.3.2 HETERODYNE INTERFEROMETER

Heterodyne interferometer is generally similar to homodyne counterparts, except that a two-frequency laser source is used instead of a single-frequency one. A schematic of a single pass heterodyne interferometer is shown in Figure 1.4. The laser source typically contains two slightly distinct optical frequencies with a known split frequency. They are generated by either placing a magnetic field around the laser tube to obtain two frequencies, or combining a single frequency laser with an acousto-optic modulator, which produces another beam with a modulated frequency [11]. The two optical

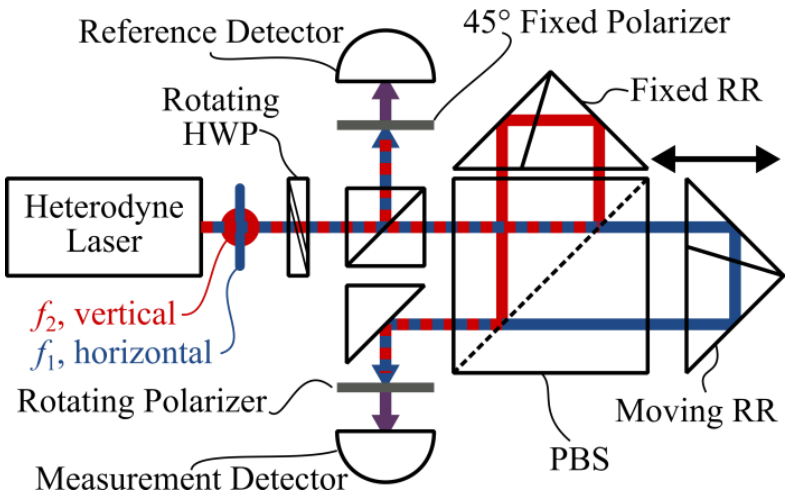


Figure 1.4 Schematic of heterodyne interferometer setup. Optical components include: retroreflectors (RR), polarizing beam splitter (PBS), polarizers, half wave plate (HWP), and photodetectors.

frequencies are orthogonally polarized and do not interfere, so they can be separated. One frequency is used in the reference arm, while another one is used in the measurement arm.

An initial beam splitter splits part of the laser output, and a polarizer causes interference between the two beams. This interference is detected at the reference detector, generating an optical reference. The main beam travels to PBS, where the frequency $f_1$ reference beam is reflected and then travels to the fixed retroreflector and back, while the frequency $f_2$ measurement beam transmits through the beam splitter and then travels to the moving retroreflector and back. The two beams are combined again within the PBS, where interference is created by passing these two collinear, orthogonal beams through this polarizer aligned at 45 °. The irradiance can be then observed at the measurement photodetector.

Heterodyne interferometer advantages:

- System has directional sensitivity.
- One optical reference can be used for multiple interferometers.
- System is insensitive to laser power fluctuations and stray light.
- System can measure fast-moving targets.
- System is adaptable to multipass configurations.

Heterodyne interferometer disadvantages:

- Two-frequency source with a split frequency is needed, increasing hardware costs.
- High speed signal processing is required.

- Polarization manipulation leads a more complex alignment procedure and costly components.

The two light waves are both linearly polarized, and have different amplitudes and frequencies. They are described by

$$\begin{aligned} E_1 &= E_{01} e^{-i(\omega_1 t+\phi_1)} \\ E_2 &= E_{02} e^{-i(\omega_2 t+\phi_2)} \end{aligned}, \tag{1.12}$$

where $\omega_i = 2\pi f_i \,(i=1,2)$ are the different angular frequencies of the light waves. When they interfere, the resultant wave, $E$, is given by the sum of the two light waves, $E_1$ and $E_2$,

$$E = E_1 + E_2 = E_{01} e^{-i(\omega_1 t+\phi_1)} + E_{02} e^{-i(\omega_2 t+\phi_2)}, \tag{1.13}$$

The resultant irradiance, $I$, is proportional to the square of the amplitude,

$$\begin{aligned} I \propto |E|^2 &= \left| E_{01} e^{-i(\omega_1 t+\phi_1)} + E_{02} e^{-i(\omega_2 t+\phi_2)} \right|^2 \\ &= \left( E_{01} e^{-i(\omega_1 t+\phi_1)} + E_{02} e^{-i(\omega_2 t+\phi_2)} \right)\left( E_{01}^* e^{-i(\omega_1 t+\phi_1)} + E_{02}^* e^{-i(\omega_2 t+\phi_2)} \right), \\ &= |E_{01}|^2 + |E_{02}|^2 + 2\,\mathrm{Re}\left( E_{01} E_{02}^* e^{-i(\Delta\omega t+\Delta\phi)} \right) \\ &= I_1 + I_2 + 2\sqrt{I_1 I_2}\cos\left(\Delta\omega t + \Delta\phi\right) \end{aligned} \tag{1.14}$$

where $\Delta\omega = \omega_1 - \omega_2$. Comparing Equation 2.9 with Equation 2.14, now there is an additional term, frequency difference $\Delta\omega$, referred as to split or beat frequency, which results from two slightly different optical frequencies. In the heterodyne interferometer, the irradiance is measured by the fluctuation at the split frequency. The displacement of the moving target causes phase change, $\Delta\phi$. Measurement of this phase change is proportional to the displacement. The output of the heterodyne interferometer occurs at

some frequency around the split frequency. Therefore, the sign of the frequency shift can describe the direction of the motion.

## 1.4 ERRORS AND UNCERTAITY IN HETERODYNE INTERFEROMETRY

This section introduces typical errors and uncertainty in a heterodyne interferometer system. Their source and correction or compensation methods are discussed. Measurement uncertainty can be attributed to several sources, and the four primary categories are displacement-dependent sources, alignment and setup sources, environmental sources, and bandwidth sources. Each uncertainty source can be present in more than one category.

### 1.4.1 REFRACTIVE INDEX UNCERTAINTY

The uncertainty in the refractive index is typically the dominant uncertainty in displacement measurements in air. The refractive index of a medium is a function of its density. It is necessary to identify the local refractive index since most interferometer applications operate in air.

For interferometry in air, the uncertainty in the refractive index occur due to changes in temperature, pressure, humidity, and gas composition, which degrade measurement accuracy. The refractive index uncertainty in air can be determined by

$$u\left(n_{air}\right)=\sqrt{K_T^2u^2\left(T\right)+K_P^2u^2\left(P\right)+K_H^2u^2\left(H\right)}, \tag{1.15}$$

where $u\left(T\right)$, $u\left(P\right)$, $u\left(H\right)$, and $K_T$, $K_P$, $K_H$, are uncertainties and sensitivities of temperature, pressure, and humidity, respectively. The atmospheric error, which is caused by refractive index uncertainty, can be expressed as

$$e_{atm} = u\left(n_{air}\right) \times d \,, \tag{1.16}$$

where $u\left(n_{air}\right)$ is the refractive index uncertainty in air, and $d$ is the moving target displacement. The error is often the largest component in the error budget, so it must be compensated, based on the measurement of air pressure, temperature, and relative humidity [12].

### 1.4.2 COSINE ERROR

An angular misalignment between the beam direction and the average line of motion of the target results in cosine error in an interferometer with a cube corner target. Because the magnitude of this error is proportional to the cosine of the misalignment angle it is called "cosine error" [1]. Cosine error with an angle $\alpha$ between the beam and motion direction is shown in Figure 1.5. It is described as

$$e_A = l_m - l = l\left(\cos\alpha - 1\right) \approx -l\frac{\alpha^2}{2} \,, \tag{1.17}$$

where $l$ is the actual displacement, and $l_m$ is the measured displacement. Cosine error can be minimized by aligning the beam direction parallel to the axis of motion as close as possible.

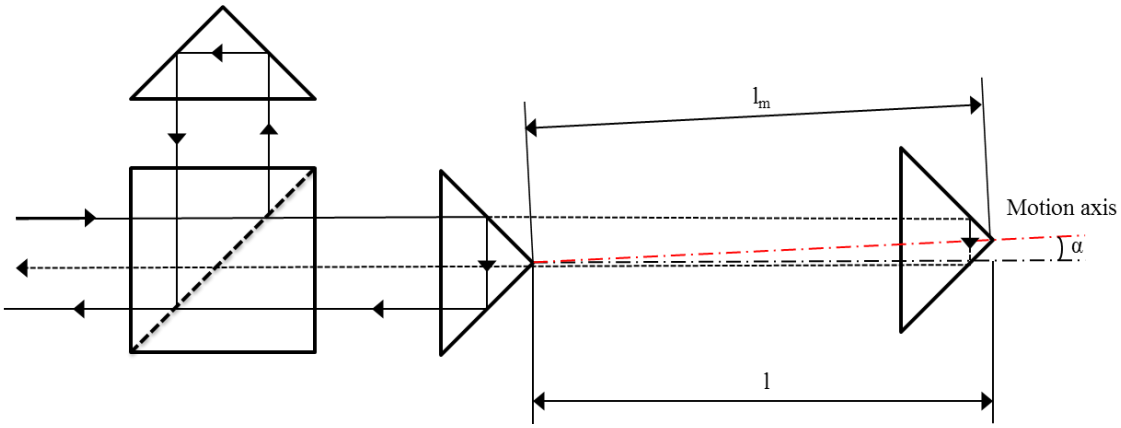


Figure 1.5 Cosine error.

### 1.4.3 ABBÉ ERROR

The Abbé principle includes arranging the measurement system to be collinear with the measured line. An offset error (Abbé error) is caused by the unintended angular error of the linear motion as the measurement axis and the motion line are not ideally collinear, as shown in Figure 1.6. Larger Abbé offset, $d_A$, leads to larger error between the measurement axis and the actual line of interest. Abbé error can be expressed as

$$e_A = l_m - l = d_A \tan\alpha_A \approx d_A\alpha_A, \tag{1.18}$$

where $\alpha_A$ is the angular misalignment. $\alpha_A$ is typically assumed small enough to simplify Abbé error to $d_A\alpha_A$. Measurement axis should coincide with line of interest to eliminate Abbé error.

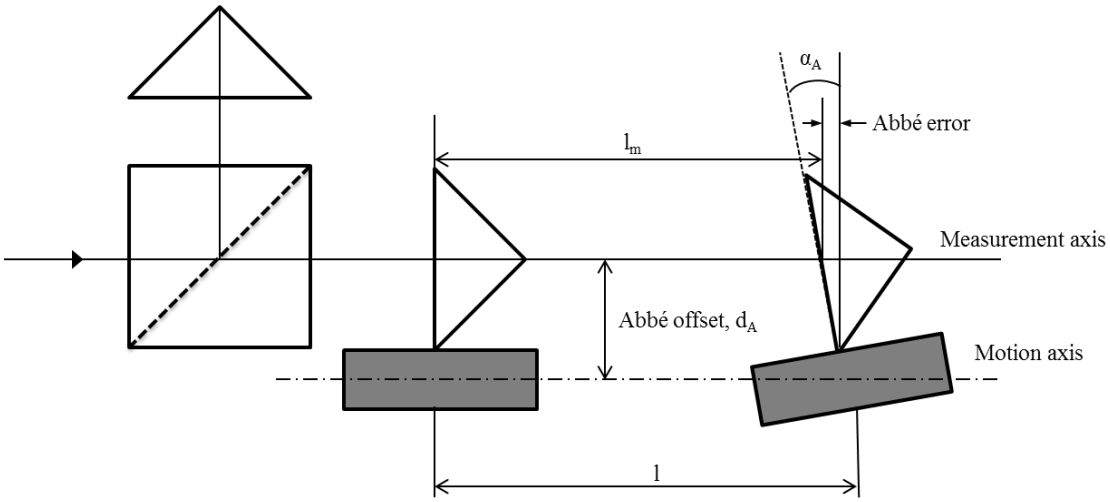


Figure 1.6 Abbé error.

### 1.4.4 PHASE CHANGE UNCERTAINTY

Uncertainty in the measured phase change is a direct contributor to the measured displacement uncertainty. Manufacturers typically provide static and dynamic accuracy instead of the phase change uncertainty. Static accuracy is generally based on the electronic noise floor. Dynamic accuracy is related to the phase meter performance at the specified target velocity. Dynamic accuracy is usually larger since nonlinearity from filter is frequency-dependent. The nonlinearity results from phase lag in the electronics and shows as an interferometric phase change. Phase delay compensation method can be applied to reduce this uncertainty [13].

### 1.4.5 INTERFEROMETER THERMAL DRIFT

Thermal changes within the interferometer optics can cause error when measuring displacement, even when the target is stationary. When temperature changes, the physical

size of the optical components will also change, which leads to an apparent displacement. The thermal drift error can be described as

$$e_{TD} = C_T \Delta T \,, \tag{1.19}$$

where $\Delta T$ is the temperature change, and $C_T$ is the thermal drift coefficient. Interferometer thermal drift can be reduced by either choosing a temperature-insensitive optical configuration or keeping the environment temperature consistent during experiment.

### 1.4.6 MATERIAL THERMAL EXPANSION ERROR

Due to thermal expansion or contraction, mechanical component dimension varies as the change in temperature. It needs to correct based on the temperature information of the part and coefficient of linear thermal expansion.

### 1.4.7 DEADPATH ERROR

The interferometer deadpath is the difference in length between the reference and measurement arms when the interferometer electronics are initialized. Figure 1.7 shows a traditional linear interferometer with imbalanced arm lengths. The path of the measurement beam is larger than that of the reference beam by the deadpath length, $d_{DP}$. Any uncompensated refractive index change over the deadpath causes an apparent displacement even when the target is not moving. Deadpath error can be expressed as

$$e_{DP} = u\left(n_{air}\right) \times d_{DP} \,. \tag{1.20}$$

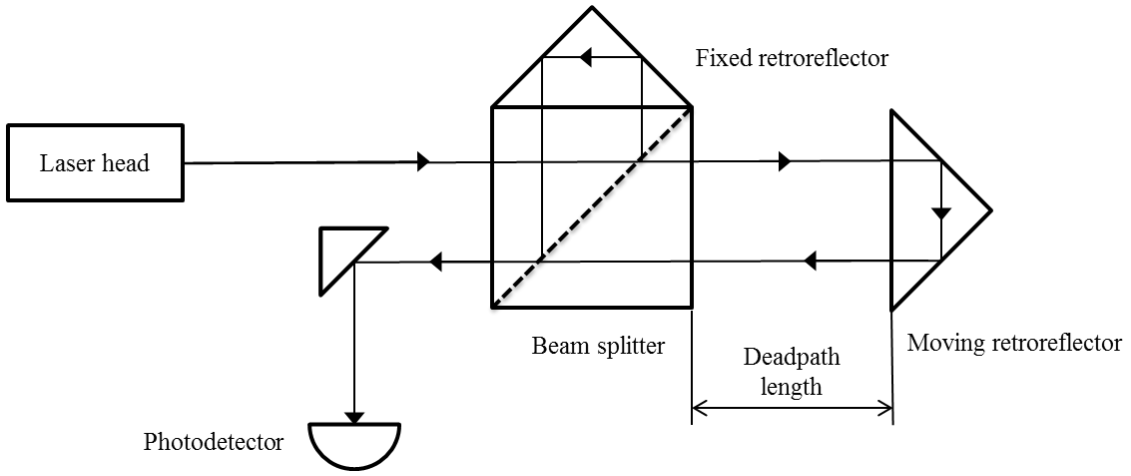


Figure 1.7 Deadpath error.

### 1.4.8 ELECTRONICS ERROR

The phase change between measurement and reference arms is measured for displacement in a heterodyne interferometer. The optical measurement resolution, i.e. one fringe, can be electrically or optically extended. The electronics measurement resolution is determined by the number of points in one full cycle of the phase. The electronics error is equal to the electronics measurement resolution. However, amplifier nonlinearity may also be considered [14].

### 1.4.9 PERIODIC ERROR

Periodic error is a noncumulative error in the measured displacement from spurious interference signal arising from source mixing and beam leakage. Imperfect separation of two frequencies into the measurement and reference beam produce periodic error, or errors of some cycles per wavelength of optical path change. From another perspective, the measured moving target displacement within superimposed periodic

error can be treated as cyclically oscillating about the nominal displacement, typically with amplitude of several nanometers [15].

Ideally, the phase-to-displacement relationship is assumed to be linear, but due to the spurious interference signal, in practice, there exists a cyclic deviation and this assumption becomes incorrect since the relationship is nonlinear.

Periodic error occurs at predictable interval. First order periodic error has one harmonic per full cycle of phase change, second periodic error has two harmonics per full cycle of phase change, etc.

Periodic error characteristics can be described as:

- Periodic error does not scale with measured displacement. Source mixing and frequency leakage cause periodic error superimposed in the true displacement to be predictable.
- Periodic error is a function of interferometer geometry and the source wavelength, detectable as first, second, and higher spatial harmonics as the target moves.
- Each order of periodic error is caused by different mixing errors and alignment.

Sources of frequency mixing and leakage include non-orthogonality between the linear beam polarization, elliptical polarization of one beam, imperfect optical components, parasitic reflections from the surface, and mechanical misalignment in the interferometer [16]. For a motion of a moving retroreflector in a single pass interferometer, for example, Figure 1.8 displays a simulated displacement of this motion from 25 μm to 30 μm with a velocity of 50 mm/min in 0.006 s, and superimposed

periodic error with a first order magnitude of 4 nm and second order magnitude of 2.5 nm. The nominal constant velocity motion is extracted to reveal only the remaining periodic error component.

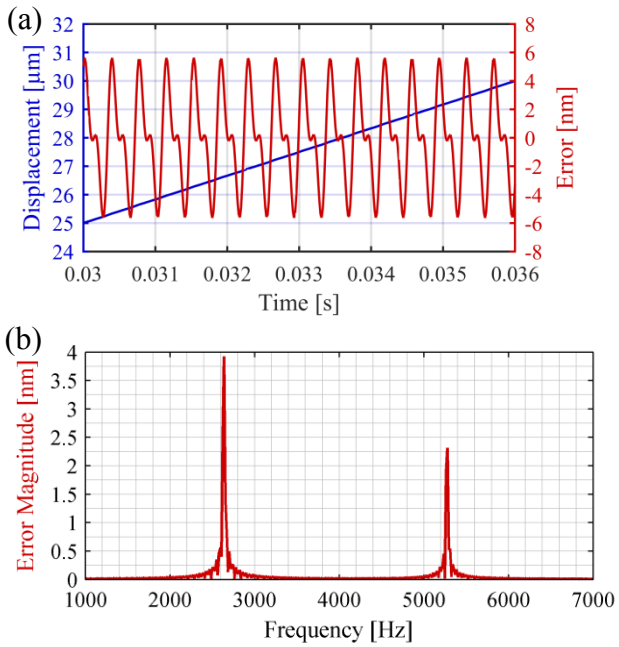


Figure 1.8 (a) Simulated linear displacement at 50 mm/min and periodic error with magnitudes of 4 nm and 2.5 nm for first and second order, respectively. (b) Periodic error amplitudes in the frequency domain.

## 1.5 PERIODIC ERROR REVIEW

Periodic error is a fundamental accuracy limitation for the heterodyne Michelson-type interferometer. It can limit the interferometer accuracy to the nanometer or subnanometer level. The measurement and reference beams are linearly polarized and mutually orthogonal, separated and recombined perfectly at polarizing beam splitter. Errors and defects in the optical system components cause source mixing and frequency leakage between the two beams. This frequency mixing causes periodic error

superimposed on the measured displacement signal, which is extensively explored in the literature.

Fedotova [17], Quenelle [18], and Sutton [19] first investigated periodic error in heterodyne Michelson-type interferometers. Subsequent studies of periodic error in displacement measuring interferometry and its reduction have been reported in many publications [1-7, 11, 14, 16, 20-90]. They are divided into the following categories: 1) error sources [1-3, 11, 20-22]; 2) refractive index in air [23-29]; 3) periodic error description and modeling [14, 30-47]; 4) periodic error measurement under various conditions [7, 48-55]; 5) periodic error correction and compensation [6, 16, 38, 56-85]; 6) uncertainty evaluation of interferometric displacement measurement [4, 5]; 7) measurement applications [86-90].

Optical mixing is a major source causing periodic error in heterodyne Michelson-type interferometers that rely on polarization coding. Optical mixing refers to part of one arm frequency leakage into the other of the interferometer. This includes imperfect optical components, mechanical misalignment between interferometer elements, non-orthogonality of linear beam polarizations, ellipticity in the nominally linear polarization of the individual beam, deviation of the optics from ideal behaviors, and parasitic reflections from individual surface.

Further, optical mixing can be subdivided into two kinds based upon the mechanism of mixing, polarization mixing and frequency mixing [1]. For polarization mixing, it is due to the imperfect separation of the beams on their polarization (due to leakage in the beam splitter). On the other hand, frequency mixing is due to contamination by correct polarization but incorrect frequency for light. It can be caused

by imperfect angular alignment of the polarization states of the beam relative to the beam splitter direction, or ellipticity in polarization states for the individual beam. Each passage through the polarizing beam splitter attenuates the leakage term for polarization mixing, while in frequency mixing, repeated passage through the beam splitter does not affect the mixing. In both kinds of mixing, the consequence is always contamination from one beam in the interferometer into another.

In spite of the source of the optical mixing, its effect can be described in Figure 1.9. The interaction of the two beams with the PBS in a practical interferometer result in an imperfect separation of the two frequencies. Beam 1 with frequency $f_1$ and amplitude $E_{01}$ is contaminated by a small component with frequency $f_2$ and amplitude $\varepsilon_{21}$, while beam 2 with $f_2$ and $E_{02}$ is contaminated by a component with $f_1$ and $\varepsilon_{12}$. Compared to Equations 2.8-9, now the resultant output beam has four components instead of two in the ideal interferometer. The resultant irradiance can be expressed by

$$\begin{aligned} I \propto |E|^2 &= \left| E_{01}e^{-i(\omega_1 t+\phi_1)} + E_{02}e^{-i(\omega_2 t+\phi_2)} + \varepsilon_{21}e^{-i(\omega_2 t+\phi_1)} + \varepsilon_{12}e^{-i(\omega_1 t+\phi_2)} \right|^2 \\ &= \underbrace{|E_{01}|^2 + |E_{02}|^2 + |\varepsilon_{21}|^2 + |\varepsilon_{12}|^2}_{DC\ Terms} + 2\,\mathrm{Re}\Bigg\{ \underbrace{E_{01}E_{02}^* e^{-i(\Delta\omega t+\Delta\phi)}}_{Nominal\ Signal} \\ &\quad + \underbrace{\underbrace{\left(E_{01}\varepsilon_{21}^* + E_{02}^*\varepsilon_{12}\right)e^{-i(\Delta\omega t)}}_{First\ Harmonics} + \underbrace{\varepsilon_{21}^*\varepsilon_{12}e^{-i(\Delta\omega t-\Delta\phi)}}_{Second\ Harmonics}}_{Periodic\ Errors} \\ &\quad + \underbrace{\left(E_{01}\varepsilon_{12}^* + E_{02}^*\varepsilon_{21}\right)e^{i(\Delta\phi)}}_{Quasi-DC\ Terms} \Bigg\} \end{aligned} \quad . \qquad (1.21)$$

Four components combine and produce eight terms. The DC terms are the irradiance of four beams, which are self-interference. The quasi-DC terms are low-frequency irradiance variations, which originate from interference between the main component in

one beam and the contamination component in the other beam with the same frequency. It is identical to the case in homodyne interferometer, and shows a small variation close to DC. In most cases they can be considered as DC terms unless $\Delta\phi$ is close to $\Delta\omega$. The remaining three terms, $E_{01}E_{02}^{*}e^{-i(\Delta\omega t+\Delta\phi)}$, $\left(E_{01}\varepsilon_{21}^{*}+E_{02}^{*}\varepsilon_{12}\right)e^{-i(\Delta\omega t)}$, and $\varepsilon_{21}^{*}\varepsilon_{12}e^{-i(\Delta\omega t-\Delta\phi)}$, are around the split frequency. The nominal signal results from the interference between two beams, and it is the desired signal. The first harmonic term arises from the interference of the desired beam and the mixing term in a given arm. The interference result is at the split frequency since they are at different frequencies $f_1$ and $f_2$. This term can be distinguished from the nominal signal by its independence of phase. The second harmonic term arises from the interference between two mixing terms, $\varepsilon_{21}e^{-i\omega_2 t}$ and $\varepsilon_{12}e^{-i\omega_1 t}$. This result shows a negative phase dependence. Its amplitude is much smaller than that of the nominal signal. The first and second order periodic errors, which are derived from the first and second harmonic terms, can be approximately given by $\sin\left(\Delta\phi\right)$ as a simplified model of a pure sine wave [7]. When the heterodyne interferometer system is under high-speed displacement and amplifier nonlinearity is considered, high order periodic errors will emerge as Doppler shifted terms; these errors can also be modeled as pure sine waves [14]. For convenience, each order of periodic error is expressed in terms of $A\sin\theta\left(t\right)$ in the following discussions, where $t$ is the time, and $\theta$ is the phase.

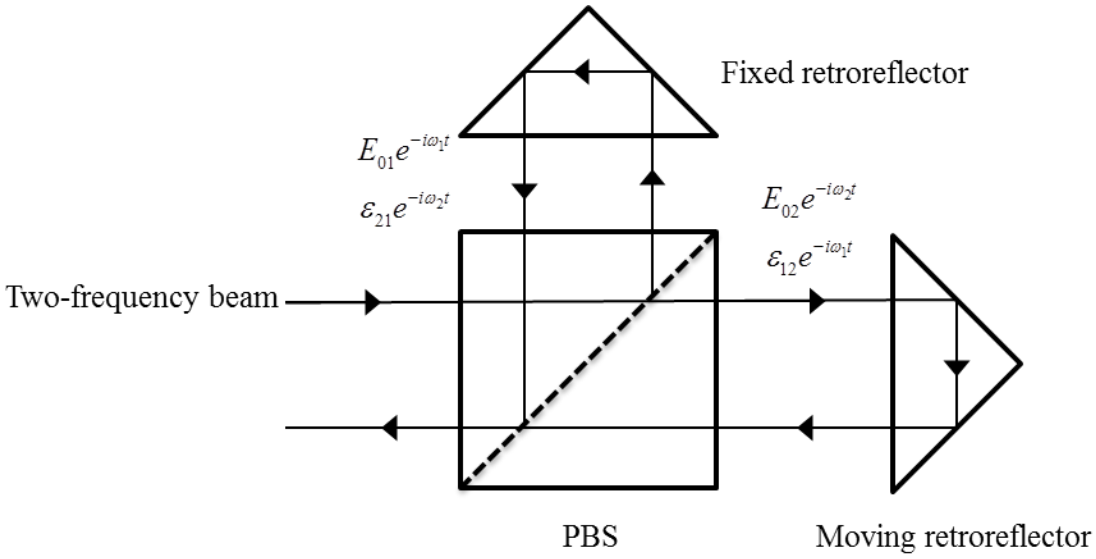


Figure 1.9 Interferometer showing optical mixing.

## 1.6 TRADITIONAL PERIODIC ERROR COMPENSATION APPROACH

As discussed in Section 1.5, the nominal, first harmonic, and second harmonic terms are $E_{01}E_{02}^{*}e^{-i(\Delta\omega t+\Delta\phi)}$, $\left(E_{01}\varepsilon_{21}^{*}+E_{02}^{*}\varepsilon_{12}\right)e^{-i(\Delta\omega t)}$, and $\varepsilon_{21}^{*}\varepsilon_{12}e^{-i(\Delta\omega t-\Delta\phi)}$. If the measured moving retroreflector is at a constant velocity, $v$, then $\Delta\phi$ can be described as $\frac{2\pi Nv}{\lambda}t$, where $N$ is the number of passes in the interferometer. In this case, $\frac{2\pi Nv}{\lambda}$ is a constant. Therefore, these three terms are at constant frequencies of $\Delta\omega+\frac{2\pi Nv}{\lambda}$, $\Delta\omega$, and $\Delta\omega-\frac{2\pi Nv}{\lambda}$. The traditional frequency domain approach [6-8] can be applied here since they are all stationary signals. The periodic error amplitudes are determined by computing the Fourier transform of the time domain displacement data.

But, the limitation of this method is also apparent. For non-constant velocity motion, the Doppler frequency is varying with velocity. The frequency domain approach cannot be applied since the method inherently assumes stationary Fourier signals. Therefore, an alternative tool, for example, wavelet analysis used in this work, is needed to overcome this issue.

## 1.7 OUTLINE OF THE STUDY

In this study, Chapter 2 introduces the advanced signal processing tool, wavelet analysis. Different wavelet families are given and emphasis is on the complex Morlet wavelet, which is used as the main choice in the periodic error compensation algorithm design. The wavelet transform in its general form, and its relative terms and properties, are also provided. In Chapter 3, the entire compensation algorithm design process is introduced in detail. Based on the periodic error model, the periodic error information is identified by using the continuous wavelet transform. The use of wavelets allows periodic error to be reconstructed and compensated from original displacement data. Chapter 4 provides detailed simulation and experiment results using the novel compensation algorithm. Identification of separate periodic error information and overall compensation performance are both given. The effectiveness of the wavelet-based approach to detecting and compensating periodic error is compared to the traditional Fourier-based approach for constant velocity motion. Chapter 5 summarizes the results using the novel wavelet-based approach and indicates directions for future investigations.

# CHAPTER 2

## WAVELET ANALYSIS

Wavelet analysis began in the mid-1980s where it was first used to examine seismic signals. At the beginning of 1990s, wavelet analysis was recognized as a useful tool in science and engineering, and began rapidly developing during that decade. The wavelet transform has been found to be particularly useful for analyzing aperiodic, noisy, intermittent, and transient signals. It can examine a signal in both time and frequency domain, which is distinctly different from the traditional Fourier transform. A number of wavelet-based methods have been created to identify signals based on this advantage. Wavelet analysis has been applied to many research areas, including condition monitoring of machinery, video image compression, seismic signal denoising, characterization of turbulent intermittency, analysis of financial indices, etc.

### 2.1 INTRODUCTION

Wavelet analysis has been developed to be an analytical tool for signal processing, mathematical modeling, and numerical analysis. Early work was in the 1980's by Morlet, Grossmann, Meyer, Mallat, and others, and the paper by Ingrid Daubechies in 1988 first directed the attention of the larger applied mathematics communities in signal processing and statistics to wavelet analysis [91-96]. Early work was related to a specific application, and now the theory is abstracted from applications and developed on its own. One

modern wavelet research goal is to create a set of basic functions and transforms describing a function or signal. Work done by Donoho, Johnstone, Coifman, and others explained why wavelet analysis is versatile and powerful and showed wavelet system is optimal for numbers of problems [97]. Multiresolution is another important idea. Wavelets are called "The Mathematical Microscope" since discrete wavelet transform can decompose a signal at independent scales and conduct this in a quite flexible way which is superior to other methods for processing, denoising, and compression [98, 99]. Because of this advantage, signal processing in wavelet domain provides many new methods for signal detection, compression, and filtering [97, 100-104].

The wavelet transform includes the discrete wavelet transform (DWT) and the continuous wavelet transform (CWT). DWT is usually used for compression, filtering, and denoising, while the CWT is preferred to provide interpretable multi-scale information of signals. The next two sections introduce these two transforms separately.

## 2.2 DISCRETE WAVELET TRANSFORM

A signal $f(t)$ can be better analyzed if expressed as a linear decomposition

$$f(t) = \sum_l a_l \psi_l(t), \tag{2.2}$$

where $l$ is an integer index for the finite or infinite sum, $a_l$ is the real-valued expansion coefficient, and $\psi(t)$ is a set of the real-valued functions of $t$ (expansion set). An unique expansion set is called a "basis". If the basis is orthogonal, i.e.

$$\langle \psi_k(t), \psi_l(t) \rangle = \int \psi_k(t) \psi_l(t) dt = 0 \quad k \neq l, \tag{2.2}$$

Then the coefficient $a_l$ can be calculated by

$$a_l = \left\langle f(t), \psi_k(t) \right\rangle = \int f(t)\psi_k(t)dt \,. \tag{2.3}$$

For the wavelet expansion, a two-parameter system is constructed as

$$f(t) = \sum_k \sum_j a_{j,k}\psi_{j,k}(t) \,. \tag{2.4}$$

where $a_{j,k}$ is a set of expansion coefficients. Two-dimensional families of scaling and wavelet functions are generated from the basic scaling function and mother wavelet, $\varphi(t)$ and $\psi(t)$, by scaling and translation,

$$\begin{aligned} \varphi_{j,k}(t) &= 2^{j/2}\varphi\left(2^j t - k\right) \\ \psi_{j,k}(t) &= 2^{j/2}\psi\left(2^j t - k\right) \end{aligned}, \tag{2.5}$$

where $j$ is the scale, and $k$ is the time or space location. Further, $\varphi(t)$ and $\psi(t)$ can be expressed as

$$\begin{aligned} \varphi(t) &= \sum_n h(n)\sqrt{2}\varphi(2t-n) \\ \psi(t) &= \sum_n h_1(n)\sqrt{2}\varphi(2t-n) \end{aligned}, \tag{2.6}$$

where $h(n)$ and $h_1(n)$ are low-pass filter and high-pass filter in the decomposition filters, respectively. Therefore, as a series expansion in terms of the scaling functions and wavelets, any function $g(t)$ can be given by

$$g(t) = \sum_k c_{j_0}(k)2^{j_0/2}\varphi\left(2^{j_0}t - k\right) + \sum_k \sum_{j=j_0}^{\infty} d_j(k)2^{j/2}\psi\left(2^j t - k\right), \tag{2.7}$$

where $j_0$ is the basis scale, and $c(k)$ and $d(k)$ are some sets of coefficients. These coefficients are called the discrete wavelet transform of the signal $g(t)$, and Equation 2.7 is the inverse discrete wavelet transform (IDWT). If the wavelet system is orthogonal, the coefficients can be calculated by

$$c_j(k) = \langle g(t), \varphi_{j,k}(t) \rangle = \int g(t) \varphi_{j,k}(t) dt$$
$$d_j(k) = \langle g(t), \psi_{j,k}(t) \rangle = \int g(t) \psi_{j,k}(t) dt \quad . \tag{2.8}$$

The DWT applies a pair of decomposition filters to the original time domain signal repeatedly. The low-pass filter and high-pass filter are designed to avoid any loss of information during transform process. Figure 2.1 shows a typical structure of the DWT process. For a decomposition at a single scale, the wavelet decomposition filters are applied to a signal $x(t)$ in time domain, and the output coefficients are down sampled into low-pass band (approximation band) $A_1$ and high-pass band (detail band) $D_1$. The bands are time domain signals, and they have half of samples compared to the original signal. At the next stage, the low-pass band $A_1$ is decimated into quarters, $A_2$ and $D_2$, and so on. The final output of DWT is the approximation subband of the final scale ($A_2$ in this example), and the detail subband of all the scales ($D_1$, $D_2$ and $D_3$ in the same example).

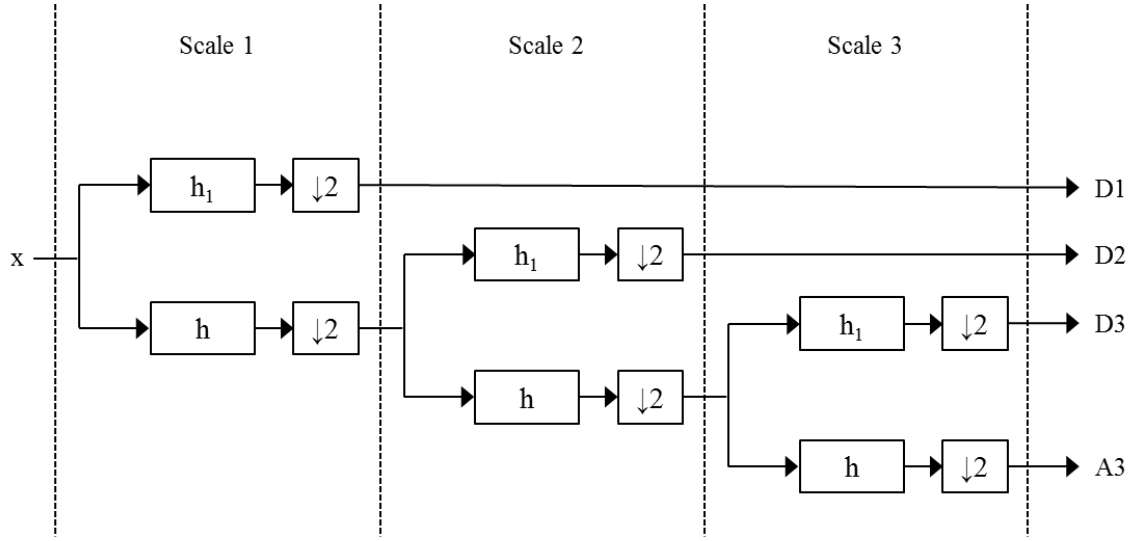


Figure 2.1 Structure of a discrete wavelet transform (DWT) computation.

However, after transforming a signal, the DWT wavelet coefficients are difficult to interpret and need an IDWT for comparison with the original signal. For CWT, in contrast, the wavelet coefficient directly provides substantial information at any particular time instance for a time domain signal. The final goal of this research is to compensate periodic error in heterodyne interferometry in real-time. Therefore, CWT is used in a real-time algorithm design to examine the spectral information of periodic error.

## 2.3 CONTINUOUS WAVELET TRANSFORM

A continuous wavelet transform is used to construct a time-frequency representation of a signal $x(t)$ which provides sufficient time and frequency localization. To perform a CWT, a wavelet is needed. It is a function $\psi(t)$ which satisfies certain mathematical criteria. This function is operated to transform the time domain signal into another form via translation and dilation.

### 2.3.1 REQUIREMENTS FOR THE WAVELET

A wavelet function of time, $\psi(t)$, must have finite energy

$$E = \int_{-\infty}^{+\infty} \left|\psi(t)\right|^2 dt < \infty . \tag{2.9}$$

A wavelet must have an average of zero,

$$\bar{\psi}(t) = \int_{-\infty}^{+\infty} \psi(t)\, dt = 0 . \tag{2.10}$$

Additionally, a wavelet is usually normalized to a unit value [105],

$$\left\|\psi(t)\right\|^2 = \int_{-\infty}^{+\infty} \left|\psi(t)\right| dt = 1. \tag{2.11}$$

### 2.3.2 WAVELET MANIPULATIONS

In order to transfer a chosen "mother" wavelet to be a more flexible form, two basic manipulations can be performed. The wavelet function can be stretched and squeezed (dilation), or moved (translatin).

A wavelet family can be generated from the mother wavelet by translating it via the shift parmeter, $u \in \Re$, and dilating the wavelet via the scale parameter, $s > 0$. This series of wavelets can be denoted as

$$\psi_{u,s}(t) = \psi\left(\frac{t-u}{s}\right). \tag{2.12}$$

The movement of the wavelet along the time axis is governed by the shift parameter. Figure 2.2(a) displays the movement of the real part of the Morlet wavelet from $u = 0$ via $u = 1$ to $u = 2$ along the time axis. The dilation and contraction of the wavelet is governed by the scale parameter, which is the distance between the center of the wavelet and the origin of time axis. Figure 2.2(b) shows the real Morlet wavelet stretched and squeezed to half and double of its original width, respectively.

### 2.3.3 WAVELET TRANSFORM

In the form of Equation 2.12, the wavelet transform of a continuous signal, $x(t)$, with respect to a wavelet function is defined as

$$Wx(u,s) = w(a)\int_{-\infty}^{+\infty} x(t)\psi_{u,s}^{*}(t)\,dt = w(a)\int_{-\infty}^{+\infty} x(t)\psi^{*}\left(\frac{t-u}{s}\right)dt, \tag{2.13}$$

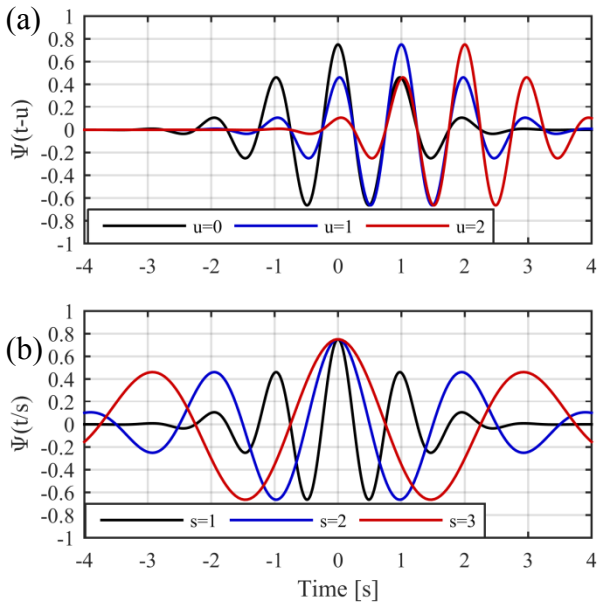


Figure 2.2 (a) Translation of the mother wavelet (the real Morlet wavelet). (b) Stretching and squeezing the real Morlet wavelet at three dilations, $s = 1, 2, 3$.

where $w(a)$ is a weighting function, and the asterisk indicates the complex conjugate of the wavelet function used in the transform, which is needed when complex wavelets are used. Typically $w(a)$ is chosen as $1/\sqrt{a}$ for energy conservation, which ensures the wavelet at each scale has the same energy. Sometimes $1/a$ is also adopted in some special applications.

In the following discussion, $w(a) = 1/\sqrt{a}$ is used as the weighting function. Thus the wavelet transform is written as

$$Wx(u,s) = \frac{1}{\sqrt{a}} \int_{-\infty}^{+\infty} x(t) \psi^* \left( \frac{t-u}{s} \right) dt . \qquad (2.14)$$

This is the continuous wavelet transform. The signal $x(t)$ could be a gearbox vibration signal, audio signal, or even a crack profile in the spatial domain. The normalized wavelet function can be written as

$$\psi_{u,s}^{*}(t) = \frac{1}{\sqrt{a}}\psi^{*}\left(\frac{t-u}{s}\right). \tag{2.15}$$

Equation 2.14 shows the integration in the product of the signal and the normalized wavelet. In mathematics, this is called the convolution integral. Therefore, the CWT can be described in a compact form as

$$Wx(u,s) = \int_{-\infty}^{+\infty} x(t)\psi_{u,s}^{*}(t)\,dt\,. \tag{2.16}$$

### 2.3.4 TYPICAL WAVELETS

The Haar wavelet is a sequence of rescaled square functions [106]. It is the simplest example of an orthonormal wavelet. The Haar wavelet is also known as Daubechies 1 tap wavelet. The mother wavelet of the Haar wavelet (shown in Figure 2.3) can be described as

$$\psi(t) = \begin{cases} 1 & 0 \le t < \frac{1}{2} \\ -1 & \frac{1}{2} \le t < 1 \\ 0 & otherwise \end{cases}. \tag{2.17}$$

Based on the characteristics of the Haar wavelet, it can be useful in discontinuity detection.

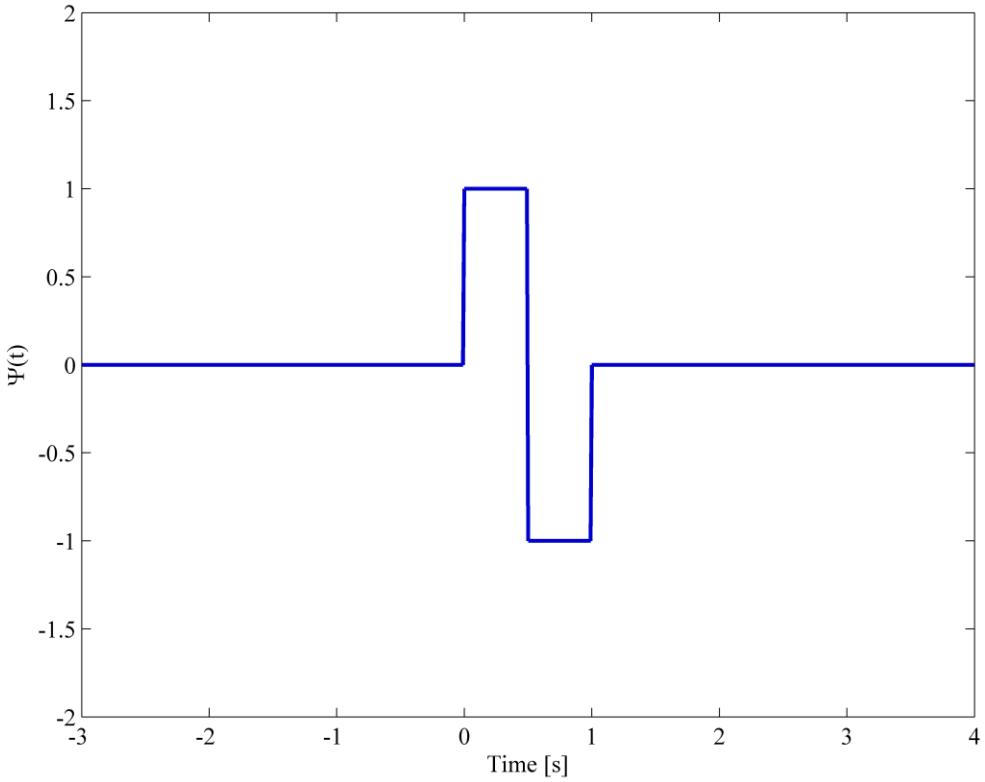


Figure 2.3 The Haar wavelet.

Hermitian wavelets are a family of continuous wavelet, which can also be used in the CWT [107]. The $n^{th}$ Hermitian wavelet is defined as the $n^{th}$ derivative of a Gaussian function,

$$\psi_n(t) = (2n)^{-\frac{n}{2}} c_n H_n\left(\frac{t}{\sqrt{n}}\right) e^{-\frac{1}{2n}t^2}, \tag{2.18}$$

where $H_n(x)$ denotes the $n^{th}$ Hermite polynomial, and the normalization coefficient is given by

$$c_n = \left(n^{\frac{1}{2}-n}\sqrt{\pi}\,2^{-n}(2n-1)!!\right)^{-\frac{1}{2}} \quad n \in \mathbb{Z}. \tag{2.19}$$

Figure 2.4 shows an example of Hermitian wavelets, which is the negative normalized first derivative of a Gaussian function,

$$\psi_1(t) = \sqrt{2}\pi^{-\frac{1}{4}} t e^{-\frac{t^2}{2}}. \tag{2.20}$$

Figure 2.5 displays another example of Hermitian wavelets, which is sometimes called "Mexican hat wavelet" and is the negative normalized second derivative of a Gaussian function [108],

$$\psi_2(t) = \frac{2}{3}\sqrt{3}\pi^{-\frac{1}{4}}\left(1-t^2\right)e^{-\frac{t^2}{2}}. \tag{2.21}$$

Depending on the application, all derivatives of the Gaussian function may be employed as a wavelet.

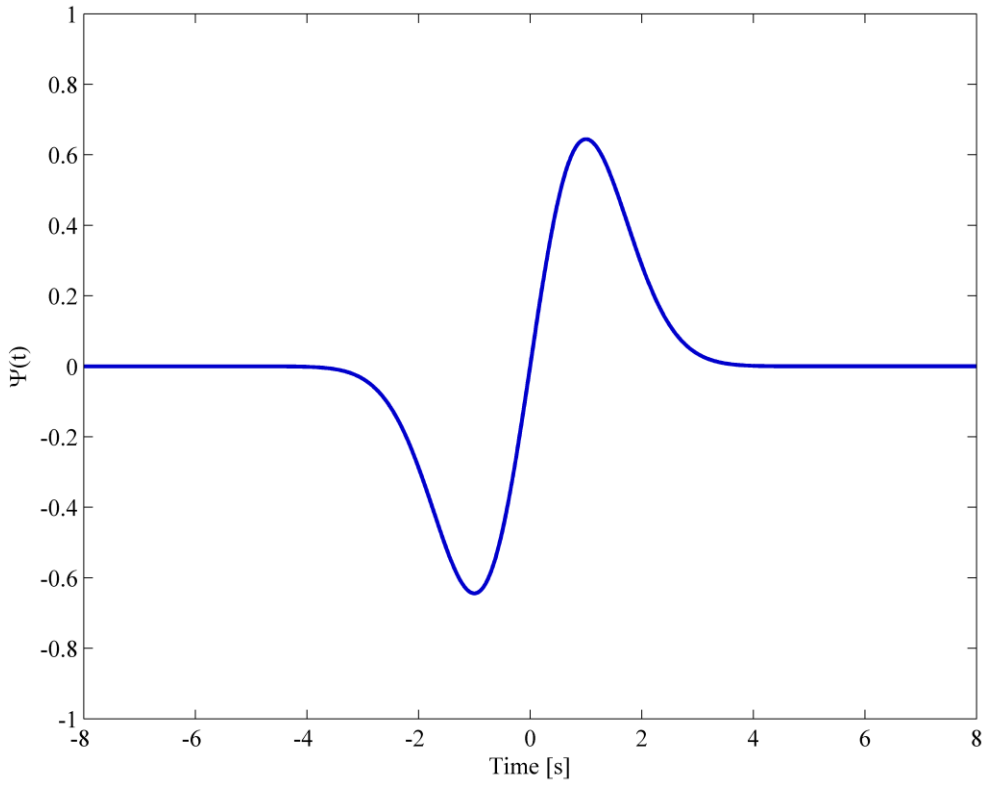


Figure 2.4 One Hermitian wavelet (first derivative of a Gaussian function).

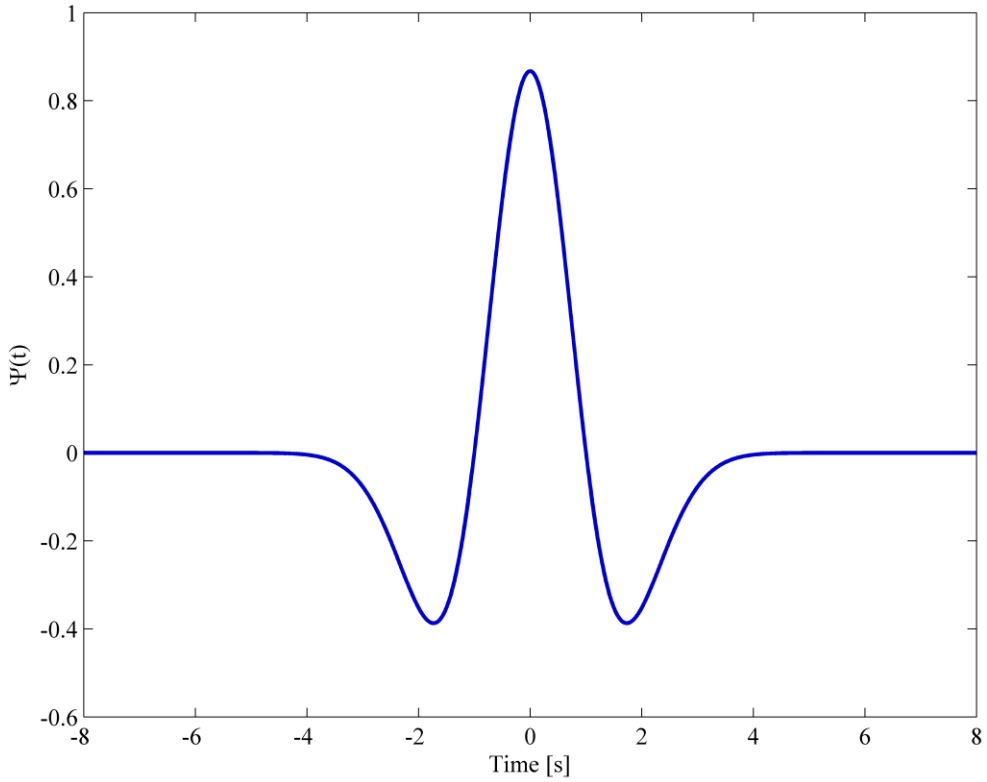


Figure 2.5 The Mexican hat wavelet.

The complex Morlet wavelet is composed of a complex exponential multiplied by a Gaussian window (shown in Figure 2.6),

$$\psi^{*}(t) = \pi^{-\frac{1}{4}} e^{i2\pi f_0 t} e^{-\frac{1}{2}t^2} . \tag{2.22}$$

where $f_0$ is the central frequency of the mother wavelet. It is closely related to human hearing and vision, and has been applied into many research fields, such as the electrocardiogram (ECG), medicine, and music transcription. More detailed introduction and analysis to the complex Morlet wavelet is given in next section.

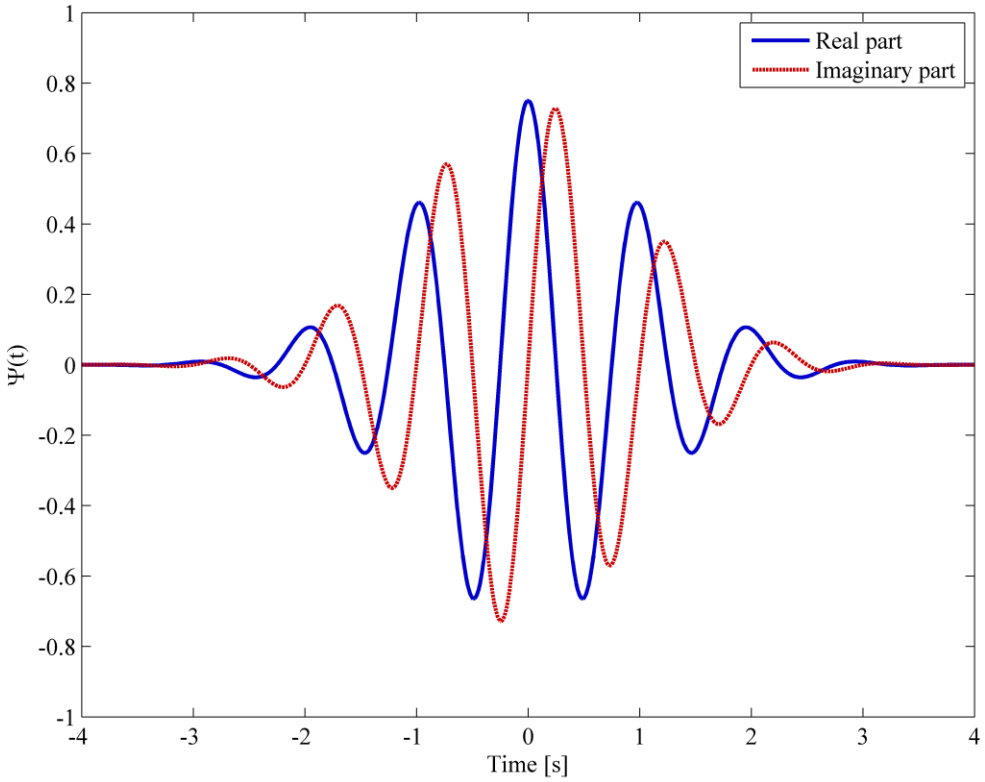


Figure 2.6 The complex Morlet wavelet.

### 2.3.5 COMPLEX MORLET WAVELET

In 1946, the use of Gaussian-windowed sinusoids for time-frequency decomposition was introduced from ideas in quantum physics. It provides the best trade-off between spatial and frequency resolution. In 1984, it was modified to keep the same wavelet shape over octave intervals, offering the first formalization of the continuous wavelet transform [109].

The shift parameter, $u$, and the scale parameter, $s$, can be included within the definition of the complex Morlet wavelet given by Equation 2.22. The shifted and dilated version of the mother wavelet can be given by

$$\psi^*\left(\frac{t-u}{s}\right)=\pi^{-\frac{1}{4}}e^{i2\pi f_0\frac{t-u}{s}}e^{-\frac{1}{2}\left(\frac{t-u}{s}\right)^2}. \tag{2.23}$$

As the wavelet is squeezed and stretched to half and double of its original width (shown in Figure 2.2b), its frequency increases and decreases to double and half of its original value.

### 2.3.6 LINEARITY PROPERTY

One property of the continuous wavelet transform is its linearity. Given a multi-component signal $x=\sum_{i=1}^{N}\alpha_i x_i$, where $x_i\left(i=1\ldots N\right)$ are signal components, and $\alpha_i\left(i=1\ldots N\right)$ are scalar weightings, the linearity states that the CWT coefficients for the signal $x$ are equivalent to the sum of the CWT coefficients for each component of $x$. In fact, the CWT is a convolution of a signal with a set of wavelets. Therefore, the foundation of this property is actually the linearity of integration. The property can be derived from

$$\begin{aligned} Wx(u,s)&=\int_{-\infty}^{+\infty}x(t)\psi_{u,s}^*(t)\,dt\\ &=\int_{-\infty}^{+\infty}\sum_{i=1}^{N}\alpha_i x_i(t)\psi_{u,s}^*(t)\,dt\\ &=\sum_{i=1}^{N}\alpha_i\int_{-\infty}^{+\infty}x_i(t)\psi_{u,s}^*(t)\,dt\\ &=\sum_{i=1}^{N}\alpha_i\left[Wx_i(u,s)\right] \end{aligned}. \tag{2.24}$$

Based on Equation 2.24, the CWT linearity property can be expressed as

$$\left(W\sum_{i=1}^{N}\alpha_i x_i\right)(u,s)=\sum_{i=1}^{N}\alpha_i\left[Wx_i(u,s)\right]. \tag{2.25}$$

It can be used to analyze the multi-component signal. The linearity is used in the periodic error compensation algorithm to obtain periodic error amplitudes (or weightings).

# CHAPTER 3

## WAVELET-BASED ALGORITHM DESIGN

In this chapter, the periodic error compensation algorithm, which is based on the continuous wavelet transform, is described by introducing all the aspects during design. In the CWT, the complex Morlet wavelet is chosen as the mother wavelet. The mathematical model of periodic error is provided, as mentioned in the Chapter 1. The CWT is discretized before using in the periodic error compensation. The important concepts in the CWT using the Morlet wavelet are also introduced. The identification methods for periodic error information (frequency, phase, and amplitude) are offered in sequence. Then all the information can be combined, aiming at compensating the periodic error in a certain constant or non-constant velocity motion profile.

### 3.1 PERIODIC ERROR MODEL

According to the discussion about periodic error in the Section 1.5, each order of the periodic error can be described as a simplified mathematical model, a pure sine wave $A\sin\theta(t)$, where $t$ is the time, $A$ is the amplitude, and $\theta$ is the phase. For example, for a periodic error, which consists of only first and second order periodic errors, can be expressed as $A_1\sin\theta_1(t)+A_2\sin\theta_2(t)$. Figure 3.1 shows first and second order periodic errors in both the time and spatial (polar coordinate) domains. The frequency, $f_1$, of the

first order periodic error is half of the second order error frequency, $f_2$. Thus, the phase, $\theta_1$, of first order periodic error is half of the second order phase, $\theta_2$.

Higher order periodic error holds the similar relationship to the first order periodic error. In general, for $k^{th}$ order periodic error $A_k \sin\theta_k(t)$, the frequency, $f_k = kf_1$, and the phase $\theta_k = k\theta_1$.

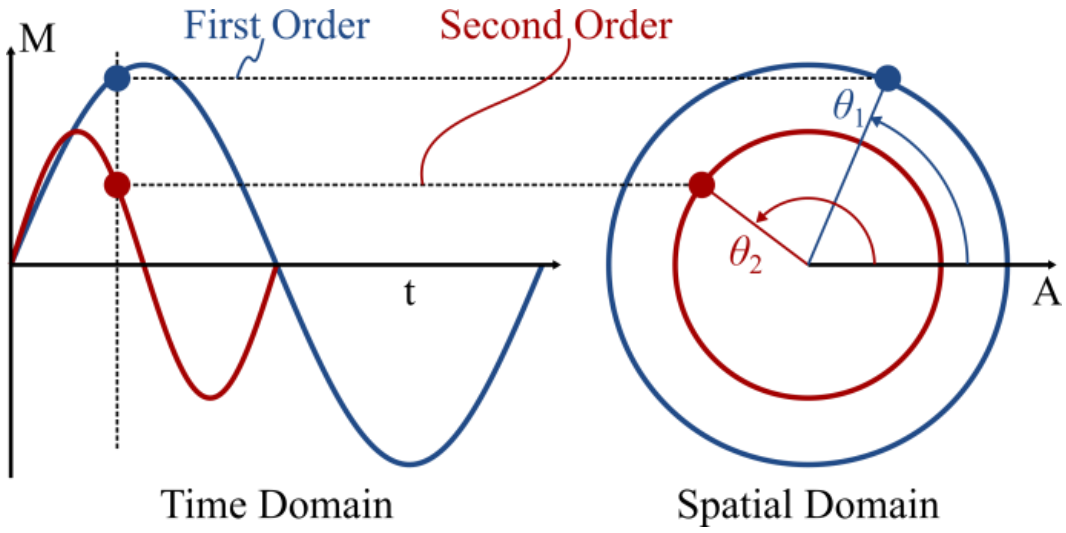


Figure 3.1. First and second order periodic error in time and spatial domain.

## 3.2 DISCRETE TIME CONTINUOUS WAVELET TRANSFORM

The data collected from real world is always digital signal. Measured displacement data by a heterodyne interferometer, for instance, is collected at a very high sampling rate (typically 50 – 100 kHz), but it is still discrete signal. For a discrete signal, the continuous wavelet transform shown in Equation 2.14 cannot be directly applied. Instead, it must be transformed to a discretized form. For a digital signal $x[1\ldots M]$ which

has $M$ data points, the discrete time continuous wavelet transform (DTCWT) can be described as

$$Wx(n,s) = \sum_{n'=1}^{M} \left( x(n') \sqrt{s} \psi^* \left( \frac{(n'-n)\Delta t}{s} \right) \Delta t \right), \tag{3.1}$$

where $x(n)$ is the $n^{th}$ discrete data point, $\psi^*$ is the mother wavelet, $M$ is the number of total data points in the signal, and $\Delta t$ is the sampling time.

## 3.3 EDGE EFFECT IN THE REAL-TIME ALGORITHM

When the algorithm is implemented to post-process a measured displacement signal, the entire signal can be directly analyzed with the DTCWT since it is already known. However, when applying the algorithm in real-time (that is, a new displacement data point is received at each sampling time), only the present and previous data points are known. The DTCWT coefficient of one data point is calculated with its neighboring points. When calculating the DTCWT at the last point of the signal, half of the wavelet is outside the signal as shown in Figure 3.2. Therefore, the DTCWT at the edges of the signal is not proportional to the DTCWT when the wavelet is almost entirely in the signal, resulting in an "edge effect".

There is no known method to eliminate this effect. However, many methods have been developed to partially resolve the issue on the edge of signals of finite extent: 1) adding a line of zero values (zero padding), a line of constant values equal to the last

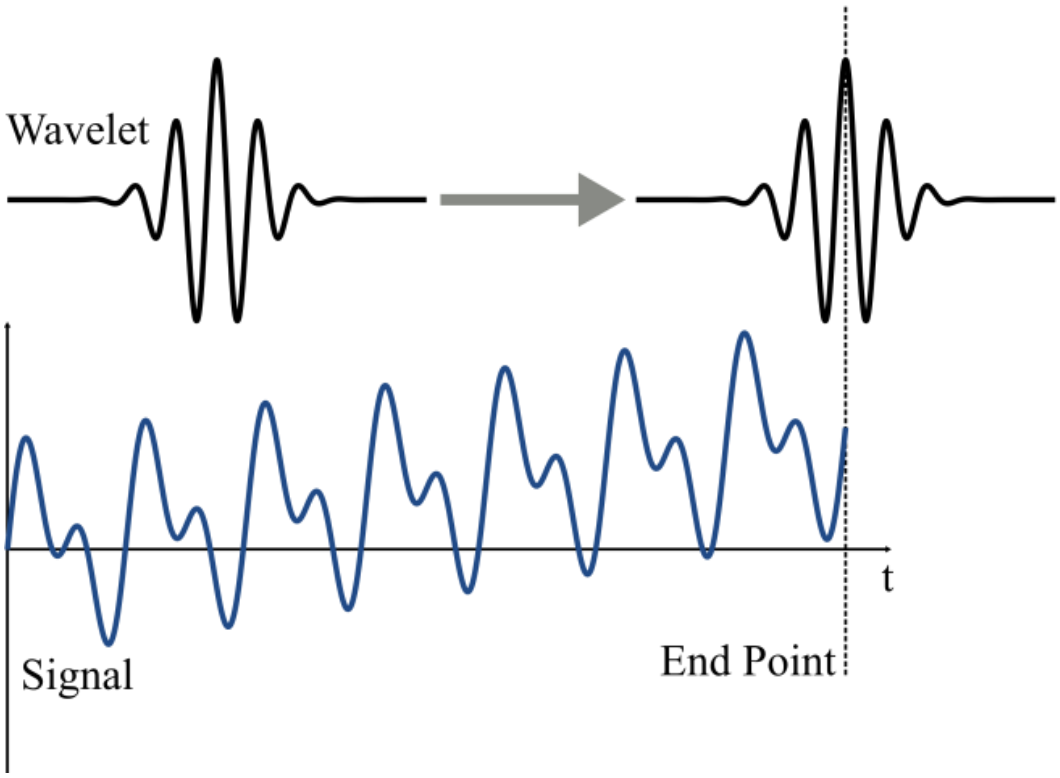


Figure 3.2. The edge effect is depicted at the end of the signal.

value of the signal (value padding), or some form of decay to zero for the last value (decay padding), at the end of the signal; 2) reflecting the signal at the edge (reflection); 3) continuing the signal on from the last point back to the first point (periodization); 4) using a polynomial extrapolation of the signal at the end (polynomial fitting). Zero padding is used in the real-time DTCWT-based periodic error compensation algorithm proposed here.

This edge effect is one main error source in the compensation algorithm. Its effect to the accuracy of periodic error information identification is discussed in the next chapter. The real-time processing algorithm is described in the next section.

## 3.4 PERIODIC ERROR COMPENSATION ALGORITHM DESCRIPTION

This section describes a detailed real-time periodic error compensation algorithm design based on DTCWT, where the complex Morlet wavelet is used as the mother wavelet. It includes periodic error identification and reconstruction.

### 3.4.1 DETREND OF THE SIGNAL

The algorithm starts with storing the latest *N* data points in a memory array, $X[1\ldots N]$, which is used as the signal to conduct the DTCWT. First, detrending $X[1\ldots N]$ is required to eliminate the main displacement component (subtracting the line connecting the beginning and ending points of the signal). This step is required because the magnitude of the periodic error is typically on the nanometer level while the overall displacement is usually on the micrometer level or larger. A new array $X'[1\ldots N]$ is obtained after detrending the measured data $X[1\ldots N]$.

### 3.4.2 APPLICATION OF THE WAVELET TRANSFORM

The DTCWT (Equation 3.1) is applied to the signal $X'[1\ldots N]$ using the following five steps:

1) substitute the data points in $X'[1\ldots N]$ for *x* in Equation 3.1;
2) select the mother wavelet to be the complex Morlet wavelet to produce child wavelets at various scales;
3) set the shift parameter n to *N* (for the last point of the array);

4) build a scale array $s[1\ldots M]$ to produce the child wavelets where $M$ is the total integer number of scales used in the DTCWT calculation;

5) using Equation 3.1 calculate the wavelet coefficient of the $N^{th}$ data point in the array.

Because the complex Morlet wavelet has complex values the resulting coefficients from the DTCWT calculation in Equation 3.1 will also be complex. Therefore, after applying the complex Morlet wavelet to the signal, the resulting wavelet transform is a complex array along the scale direction (see Figure 3.3).

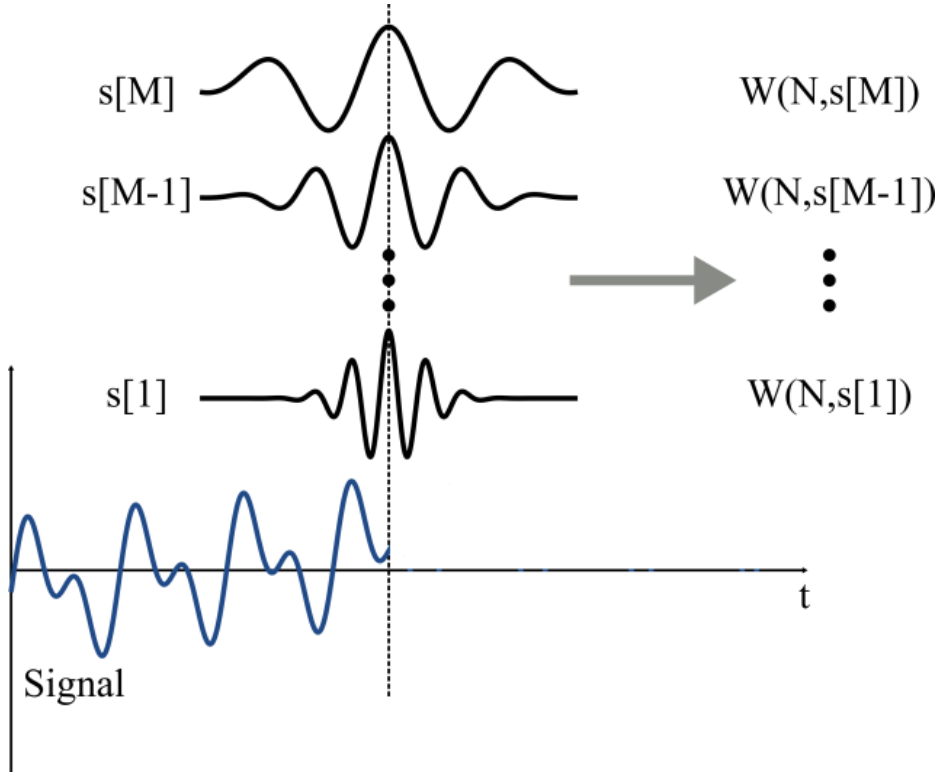


Figure 3.3. DTCWT coefficients calculation at $n = N$ and scale $s[1\ldots M]$.

### 3.4.3 IDENTIFICATION OF THE RIDGE AND PHASE

The modulus and the phase for each complex coefficient can be calculated as:

$$abs(n,s) = |Wx(n,s)| \text{ and} \tag{3.2}$$

$$\phi(n,s) = \arctan\left(\frac{\mathrm{Im}(Wx(n,s))}{\mathrm{Re}(Wx(n,s))}\right), \tag{3.3}$$

where Im and Re represent the imaginary and real parts of the DTCWT coefficient, respectively. For the modulus $abs(N,s)$ at $X'[N]$ along the scale array, the maximum value of the DTCWT coefficient or "ridge" can be extracted. The ridge is defined as the location where the modulus reaches its local maximum at scale $s_{ridge}$ [110]. When the modulus is maximal at the ridge, the frequency of the wavelet scaled by $s_{ridge}$ shows the greatest match with the convolved periodic error signal [111].

This $s_{ridge}$ equals $s_1$, which corresponds to the frequency of first order periodic error. Therefore, the phase $\phi(N, s_{ridge})$ is the first order periodic error phase at $X'[N]$. A phase array $\varphi[1\ldots N]$ is used to store this phase. A new point is added by completing two steps: 1) remove $\varphi[1]$ and shift $\varphi[2\ldots N]$ forward to $\varphi[1\ldots N-1]$ and 2) set $\varphi[N] = \phi(N, s_{ridge})$. Subsequently, the array $\varphi[1\ldots N]$ has the first order periodic error phase information for the latest *N* data points. Based on the periodic error model defined in Section 3.1, with the phase array $\varphi[1\ldots N]$ and an assumed unit amplitude, the $k^{\text{th}}$ order periodic error is $A_k \sin(\theta_k) = \sin(k\varphi)$. It is located at the scale $s_k = s_1 / k$ since its frequency is $f_k = kf_1$ and the scale is inversely related to the frequency. The $k^{\text{th}}$ order periodic error for the latest *N* points is

$$r_k[1\ldots N] = \left\{\sin(k\varphi(1)), \sin(k\varphi(2)), \ldots, \sin(k\varphi(N))\right\}, \tag{3.4}$$

which is called the “reference periodic error”.

### 3.4.4 IDENTIFICATION OF THE AMPLITUDE

The next step is to determine the amplitude of different periodic error orders. The entire periodic error $e[1\ldots N]$ is a linear combination of *m* order periodic errors, which can be expressed as

$$e[1\ldots N] = \sum_{j=1}^{m} A_j r_j[1\ldots N], \tag{3.5}$$

where $A_j\ (j = 1\ldots m)$ is the periodic error amplitude on the $j^{\text{th}}$ order, which is to be quantified.

Assuming that the detrended array, $X'[1\ldots N]$, is exactly the periodic error[1], the assumed sinusoidal combination of periodic errors $e[1\ldots N]$ can be said to be equivalent to $X'[1\ldots N]$ according to Equation 3.5 to obtain

$$X'[1\ldots N] = \sum_{j=1}^{m} A_j r_j[1\ldots N]. \tag{3.6}$$

The discrete form of the CWT in Eq. 3.1 can then be used on both sides of Eq. 3.6. Equation 3.6 is effectively substituting the actual periodic error for *x* on one side of the equation and substituting the periodic error model on the other side of the equation. Once the values are substituted the complex Morlet wavelet can be used to calculate the coefficients by setting the location to be $n = N$, and using scales $s[1\ldots M]$. The linearity

[1] If there is a difference between the detrended signal and the actual periodic error due to imperfect detrending, this causes an error in the algorithm results.

property of the CWT introduced in Eq. 2.5 can then be used to construct the following result:

$$WX'[1\ldots N](N, s[1\ldots M]) = \sum_{j=1}^{m} A_j \left[ Wr_j [1\ldots N](N, s[1\ldots M]) \right], \tag{3.7}$$

where $WX'[1\ldots N](N, s[1\ldots M])$ has already been calculated. For *m* order reference periodic errors, another *m* DTCWT calculations about $Wr_j [1\ldots N](N, s)$ $(j = 1\ldots m)$ are required. Amplitudes $A_j\ (j = 1\ldots m)$ include *m* unknowns, which require at least *m* equations to be solved. Recall that the frequency of $j^{\text{th}}$ order periodic error is related to the scale $s_j = s_1 / j$, so the DTCWT results $WX'[1\ldots N](N, s_i)$ and $Wr_j [1\ldots N](N, s_i)$ at scale $s_i$ are extracted for use $(i, j = 1\ldots m)$. Let $c_i = WX'[1\ldots N](N, s_i)$, $d_{ij} = Wr_j [1\ldots N](N, s_i)$, $i, j = 1\ldots m$. The following set of equations can then be obtained from Equation 3.7:

$$\begin{cases} c_1 = A_1 d_{11} + A_2 d_{12} + \ldots + A_m d_{1m} \\ c_2 = A_1 d_{21} + A_2 d_{22} + \ldots + A_m d_{2m} \\ \vdots \\ c_m = A_1 d_{m1} + A_2 d_{m2} + \ldots + A_m d_{mm} \end{cases} \Rightarrow \begin{bmatrix} A_1 \\ A_2 \\ \vdots \\ A_m \end{bmatrix} = \begin{bmatrix} d_{11} & d_{12} & \cdots & d_{1m} \\ d_{21} & d_{22} & \cdots & d_{2m} \\ \vdots & \vdots & \ddots & \vdots \\ d_{m1} & d_{m2} & \cdots & d_{mm} \end{bmatrix}^{-1} \begin{bmatrix} c_1 \\ c_2 \\ \vdots \\ c_m \end{bmatrix}. \tag{3.8}$$

The amplitudes $A_j\ (j = 1\ldots m)$ can therefore be determined.

### 3.4.5 RECONSTRUCTION OF PERIODIC ERROR

The magnitude $M$ of the periodic error at the latest sampling time is calculated using

$$M = \sum_{i=1}^{m} A_i \sin\left(i\varphi(N)\right), \tag{3.9}$$

where $A_i \sin\left(i\varphi\left(N\right)\right)$ is i$^{th}$ order reconstructed periodic error at $n = N$. Finally, the magnitude *M* is subtracted from the original displacement data to determine the compensated displacement data point.

Figure 3.4 displays the sequence of calculations required for compensating one displacement data point in the DTCWT algorithm.

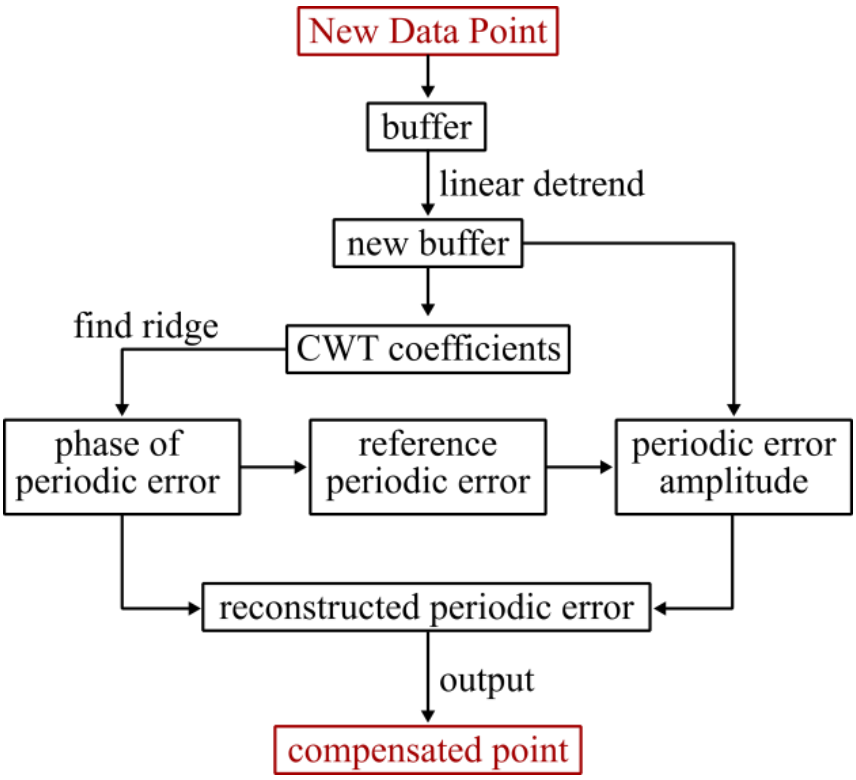


Figure 3.4. Calculations to implement the periodic error compensation algorithm.

# CHAPTER 4

## SIMULATION RESULTS

In this chapter, simulated displacement data with superimposed periodic error are used to assess the validity of the wavelet-based compensation algorithm. The simulated data is first introduced. Then identifications of periodic error ridge, phase and amplitude are provided in sequence. For the results, the influence caused by the edge effect in the algorithm, the Morlet wavelet central frequency, and the size of the memory array used in the DTCWT, is also discussed. Finally, overall periodic error compensation performance of the wavelet-based algorithm is shown. In order to demonstrate the capability of the wavelet-based approach to compensate periodic error, it is compared to the traditional Fourier-based approach.

### 4.1 SIMULATED DISPLACEMENT DATA

The simulated displacement is designed to coincide with the collected data in a real heterodyne interferometer. But more ideally, only the first and second order periodic errors are considered in the simulated data. The interferometer parameters used in the simulation are:

1) He-Ne laser wavelength of $\lambda$ = 633 nm;
2) a fold factor of $FF$ = 2, which describes the number of light passes through the interferometer (the first order error completes a full cycle in

3) 633/2 = 316.5 nm, while the second order error requires 633/4 = 158.3 nm);

4) a sampling frequency was 62.5 kHz.

A typical simulated signal used in the simulations is a linear displacement signal where first and second order periodic errors (amplitudes 4 nm and 2.5 nm, respectively) are superimposed during a constant velocity (50 mm/min) displacement as shown in Figure 4.1.

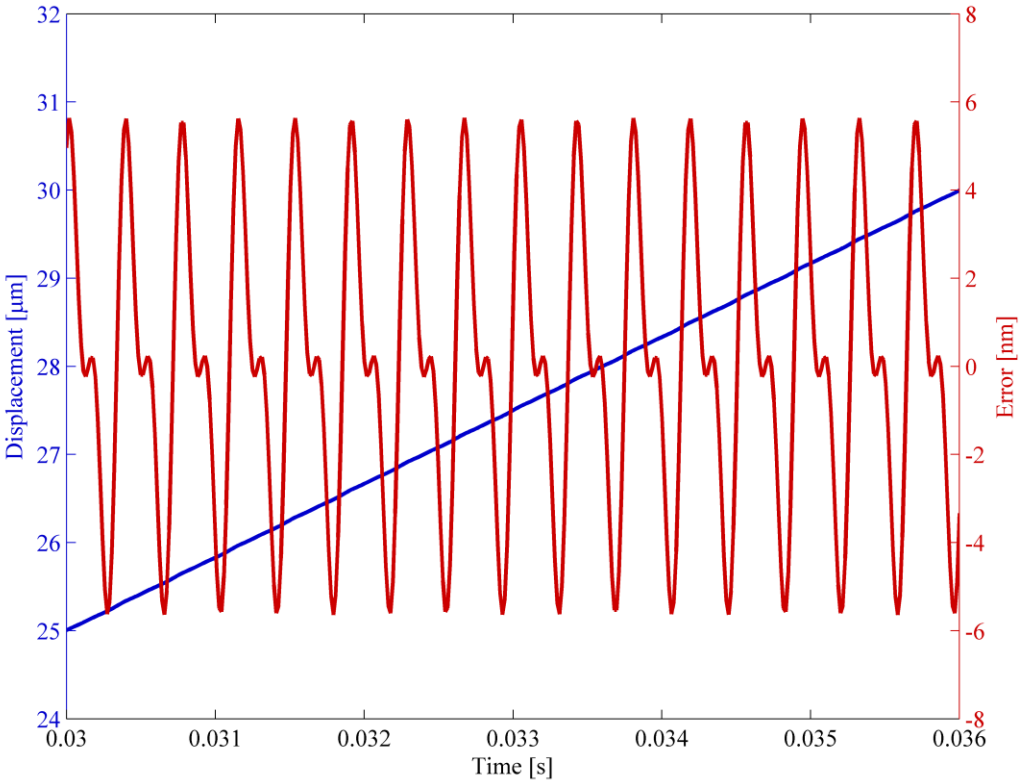


Figure 4.1 Simulated linear displacement at 50 mm/min and periodic error with magnitudes of 4 nm and 2.5 nm for first and second order.

The following sections discuss the results of ridge detection, phase detection, amplitude detection, and a comparison between the DTCWT and frequency domain approaches.

## 4.2 RIDGE DETECTION

Identifying periodic error frequency components first requires ridge detection using Equation 3.2. The performance of the ridge detection portion of the algorithm is evaluated using the simulated displacement signal shown in Figure 4.1.

The algorithm is designed to apply in the real-time displacement measuring experiment. Therefore, the edge effect always occurs as introduced in Chapter 3. Inevitably, this leads to an error. In order to illustrate this error, the same algorithm is implemented offline for comparison. In this case, the entire displacement profile is known before the algorithm runs, which means the edge effect does not exist since at each point both previous and future data points can be used in the calculation. For both algorithms (real-time and offline), the comparison results of the measured DTCWT ridge for the simulated signal is displayed in Figure 4.2. The ridge detected from the real-time algorithm is at the integer scale $190 \pm 1$, while that from the off-line algorithm is consistently at scale 190. This demonstrates that periodic uncertainty in the real-time algorithm caused by the edge effect can cause the calculated scale to differ from the actual value.

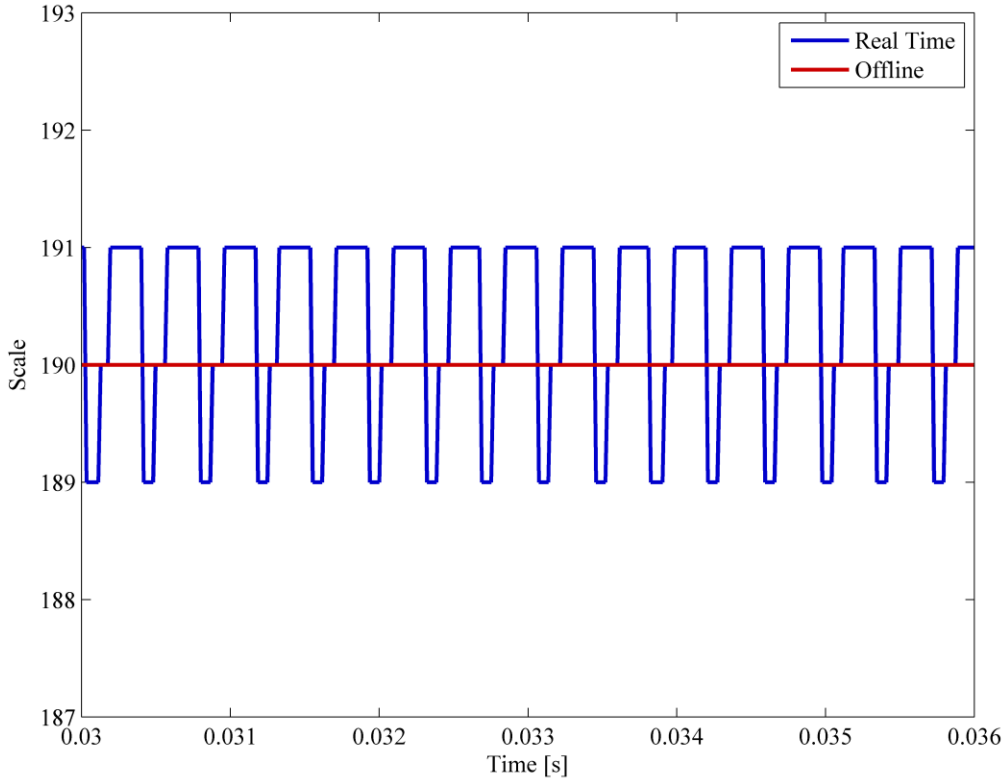


Figure 4.2 The measured DTCWT ridge for the error signal.

To ensure the calculation result is accurate enough for real-time error compensation, some parameters in the algorithm may be adjusted, such as the central frequency of the Morlet wavelet and the size of the memory array used in the DTCWT.

For the same displacement data in Figure 4.1, Figure 4.3 shows the ridge identification result when the central frequency $f_0 = 1$. The detected ridge is at the scale $25 \pm 2$. The scale is inversely related to the frequency. For two scales which have uncertainties in the same level, the smaller scale leads to a larger uncertainty of the frequency. Ridge is the location where the frequency of the Morlet wavelet is identical to that of the signal, and the Morlet wavelet frequency decreases when the scale increases as

discussed in Section 2.3.5. Therefore, to increase the measured ridge for one signal, the central frequency of the Morlet mother wavelet can be increased. Figure 4.4 shows the identified ridge when $f_0 = 8$. In this case, the measured ridge is at the scale $190 \pm 1$. The base scale increases from 25 to 190 while its uncertainty does not change much, but this dramatically reduces the frequency uncertainty. However, the central frequency cannot be raised too high because it requires higher sampling rate and this is restricted by the hardware resources. Thus, $f_0 = 8$ is used in the rest of simulations in this work.

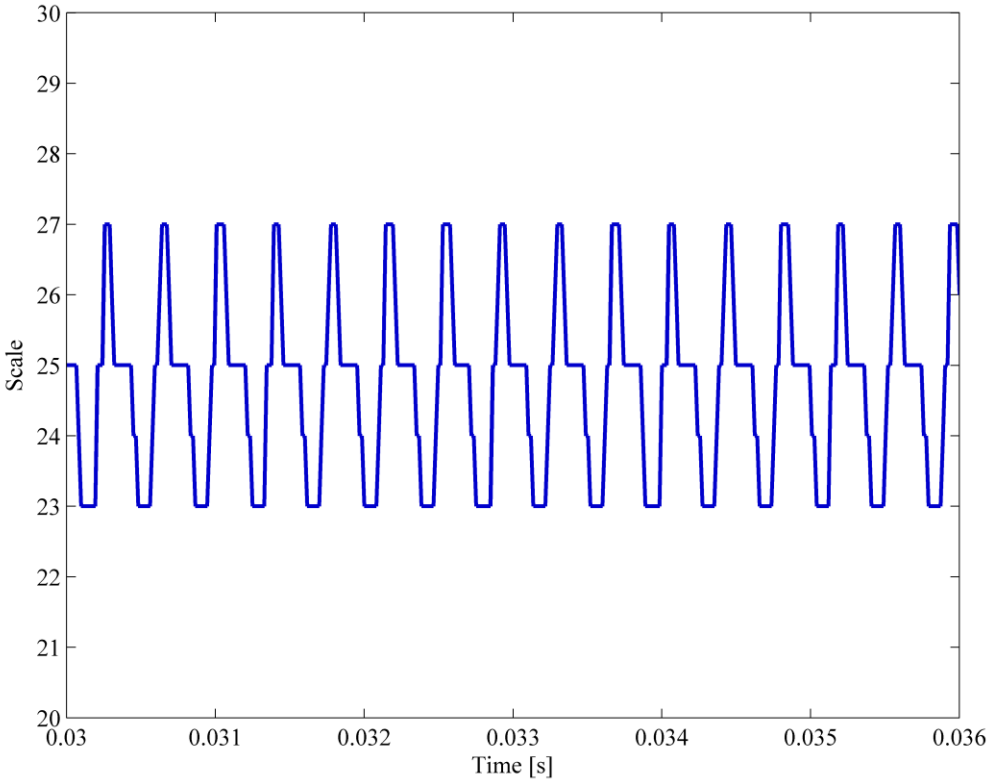


Figure 4.3 The measured DTCWT ridge ( $f_0 = 1$).

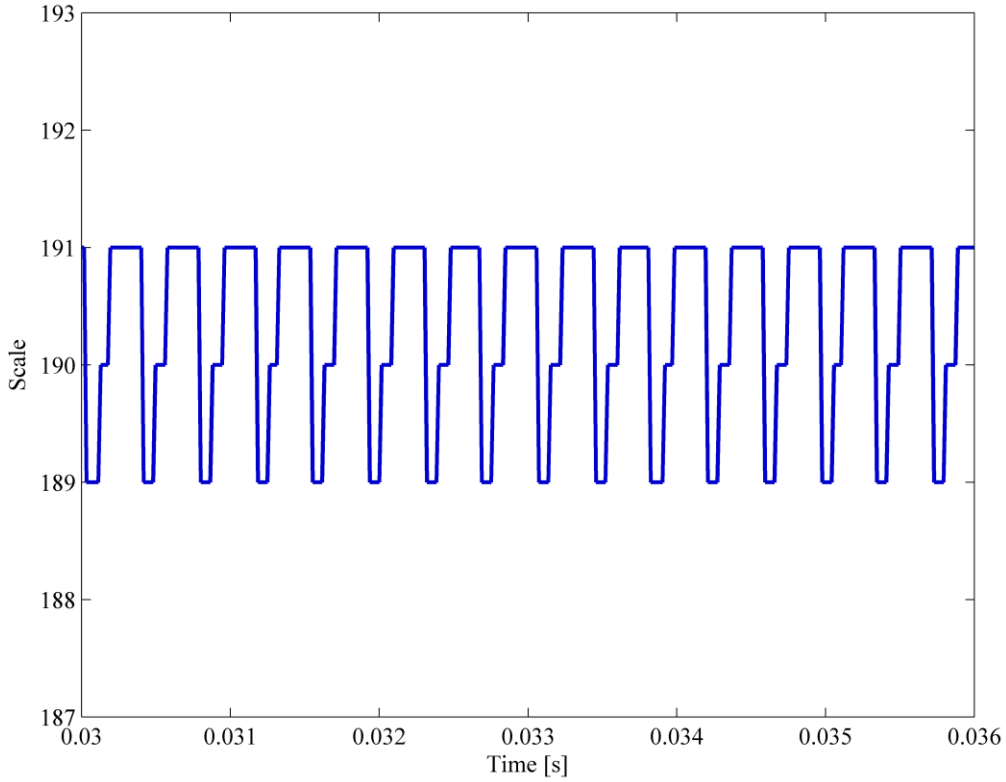


Figure 4.4 The measured DTCWT ridge ( $f_0 = 8$ ).

The size of the array used in the DTCWT, i.e. the memory array $X[1 \ldots N]$, can also be justified. The choice of this size is based on the sampling rate and the frequency of periodic error, because the array needs to include several cycles of periodic error (at least 8 – 10 cycles), in order to identify the error with high accuracy. If the sampling frequency is too high or the frequency of periodic error is too low, the array needs to be enlarged to accommodate enough periodic error cycles for calculation to achieve high accuracy in periodic error compensation. For example, when $N = 100$, the ridge identification result is shown in Figure 4.5a. It can be clearly seen from Figure 4.5b that the detected ridge is no longer related to the first order periodic error but the second

order, which means that in this situation, the size of the memory array is not enough to identify the first order periodic error frequency. Figures 4.6 and 4.7 display the cases at $N = 200$ and $N = 400$, respectively, where both results are $190 \pm 1$ for the ridge. Therefore, $N = 200$ is used in the following simulations, also based on the consideration for saving hardware resource.

## 4.3 AMPLITUDE DETECTION

For the simulations in this section, a simulated constant velocity motion (50 mm/min) with first order periodic error amplitude of 4 nm and second order periodic error amplitude of 2.5 nm is used just as in Section 4.2. To identify the periodic error amplitudes under this constant velocity condition, two methods are compared at every sampling instant. The first method is a fast Fourier transform (FFT) method similar to [6-8]. The FFT of the error is computed after detrending the nominal displacement stored in the displacement array $X[1 \ldots N]$ and applying a Hanning window. The second method is the DTCWT-based algorithm. This algorithm is applied to calculate first and second order periodic error amplitudes (Equation 3.8, where $m = 2$ because only first and second order periodic errors exist) after obtaining the modulus and phase information (Equations 3.2 and 3.3) and determining the reference periodic errors (Equation 3.4). The measured amplitudes are displayed in Figure 4.8. The frequency domain approach result is smoother since windowing reduces the spectral leakage. The FFT assumes that the data is point each sampling interval. It actually measures the average amplitude over the signal. For first order periodic error, the true value of its amplitude is 4 nm. The average value

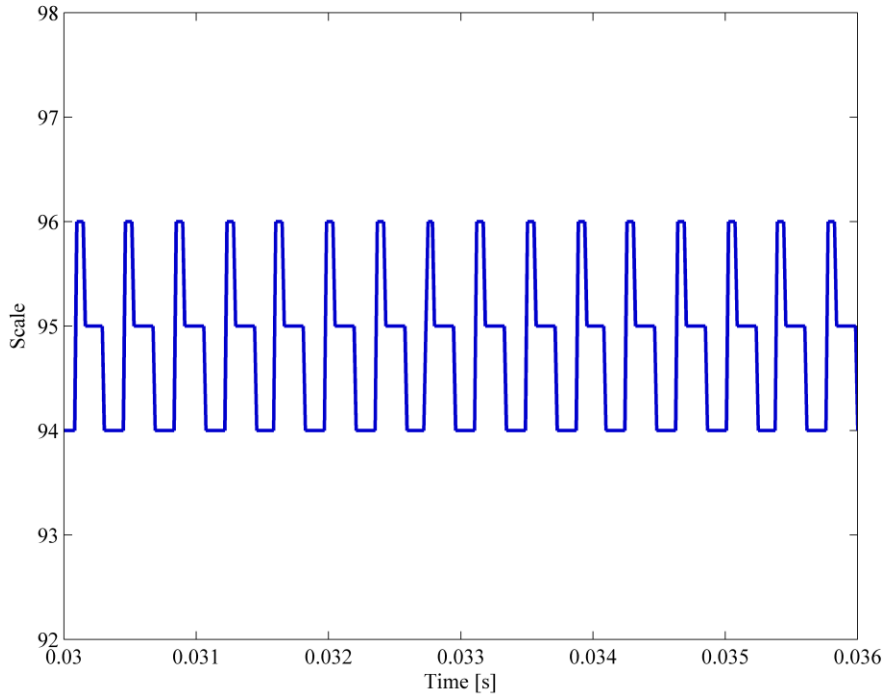


(a)

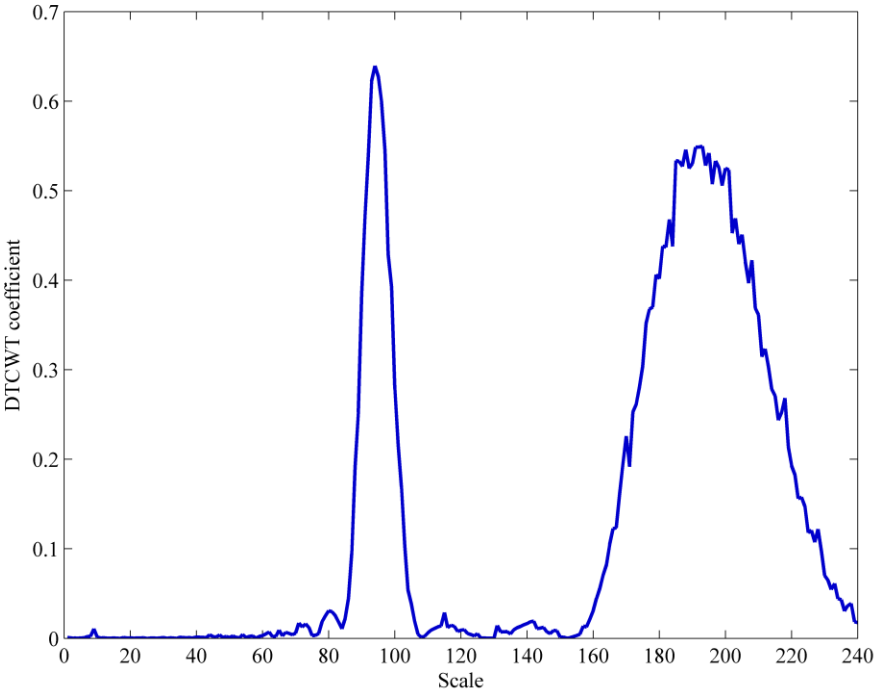


(b)

Figure 4.5 The measured DTCWT ridge ( $N = 100$ ).

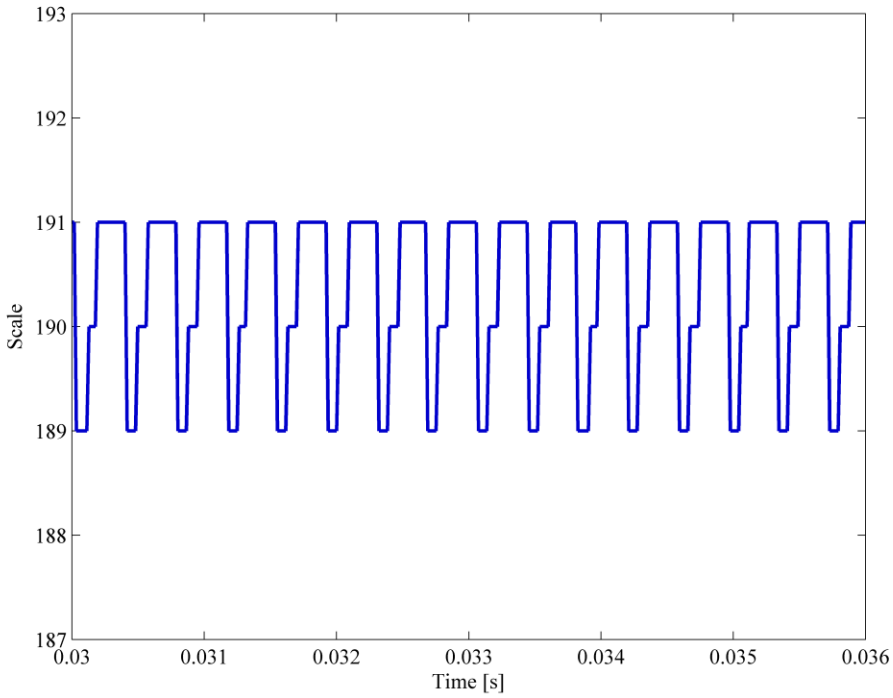


Figure 4.6 The measured DTCWT ridge ( $N = 200$ ).

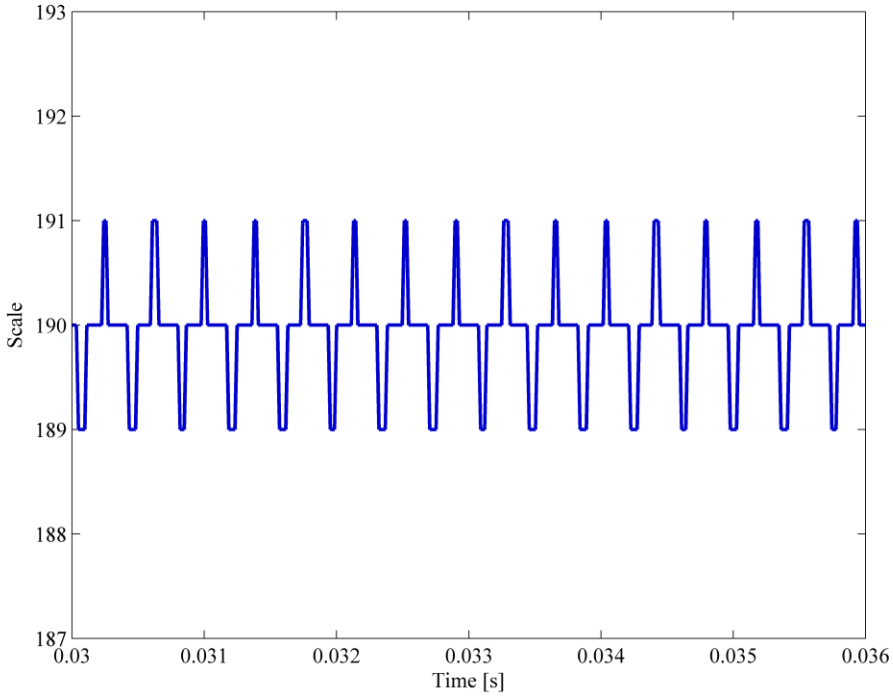


Figure 4.7 The measured DTCWT ridge ( $N = 400$ ).

from the FFT approach is 3.92 nm; the amplitude measured by the DTCWT approach is 4.25 nm. For second order periodic error, the true value is 2.5 nm. The amplitudes measured by the FFT and DTCWT approaches are 2.34 nm and 2.31 nm, respectively. The two approaches show good agreement for amplitude measurement.

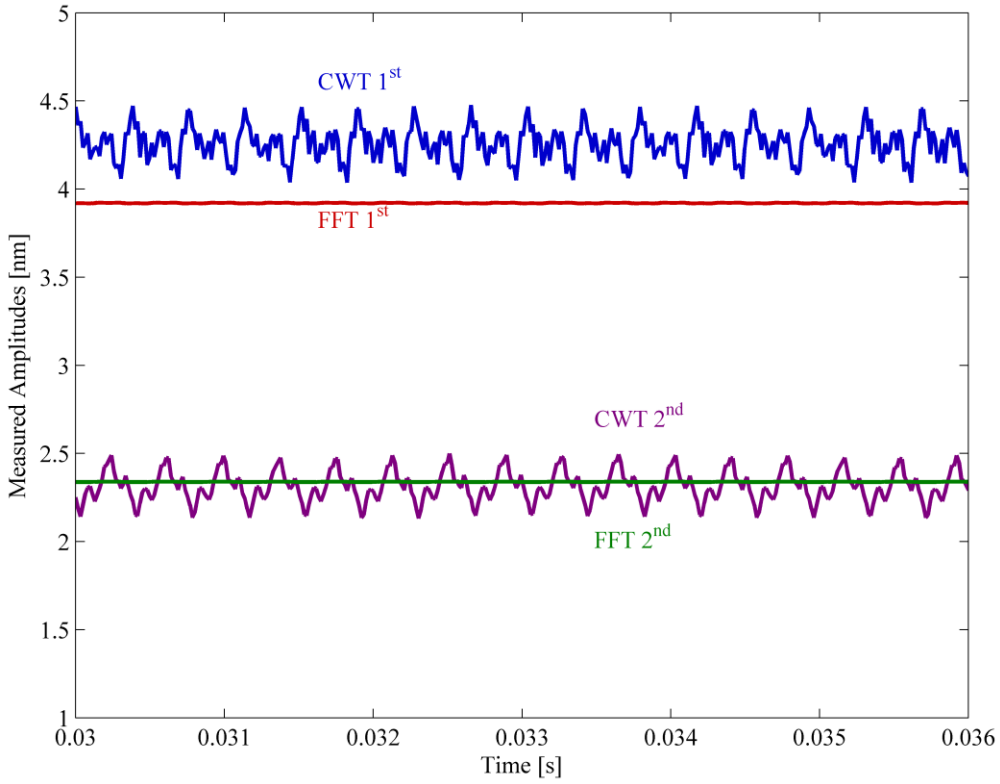


Figure 4.8 The measured amplitudes for the FFT and DTCWT approaches.

## 4.4 PERIODIC ERROR COMPENSATION

In these tests, the performance of the entire DTCWT algorithm (from receiving a new data point to providing a compensated data point) is examined. Again, the simulated 50 mm/min constant velocity motion with superimposed periodic errors is used. The time domain periodic error compensation result is displayed in Figure 4.9. The root-mean-

square error is reduced from 3.32 nm to 0.49 nm for both two methods. Figure 4.10 displays the compensation result in the frequency domain. After compensation, the amplitudes of the first and second order periodic errors are reduced from 4 nm to 0.24 nm (0.27 nm for the FFT method) and from 2.5 nm to 0.30 nm (0.27 nm for the FFT method), respectively. These similar results indicate that the DTCWT algorithm has the capability to accurately compensate the periodic error.

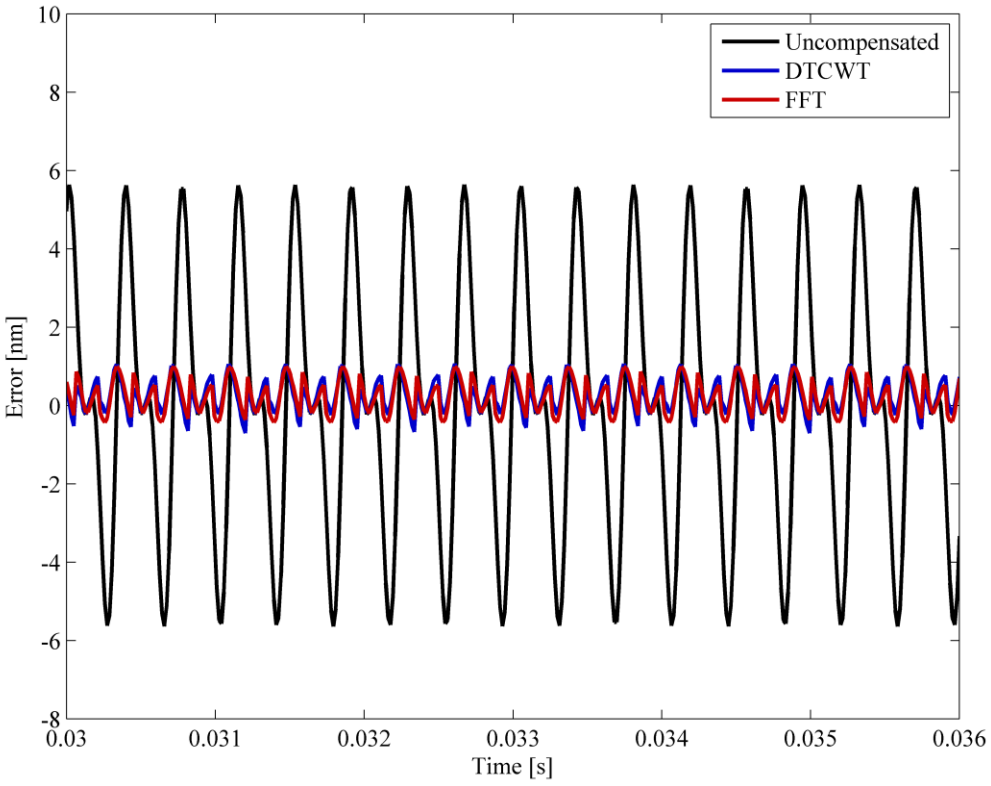


Figure 4.9 The result of periodic error compensation (both DTCWT and FFT approaches) in the time domain is displayed.

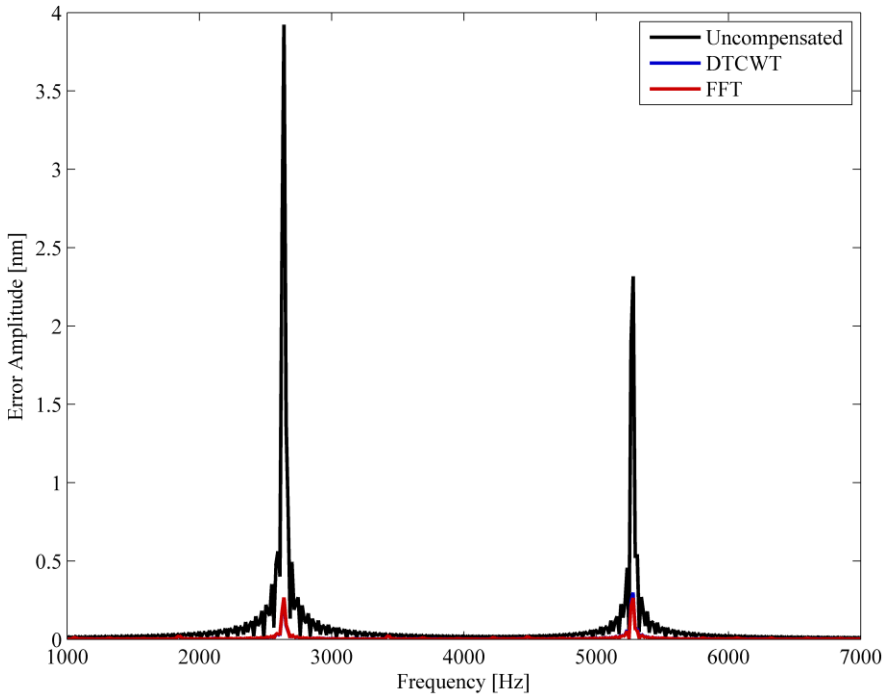


(a)

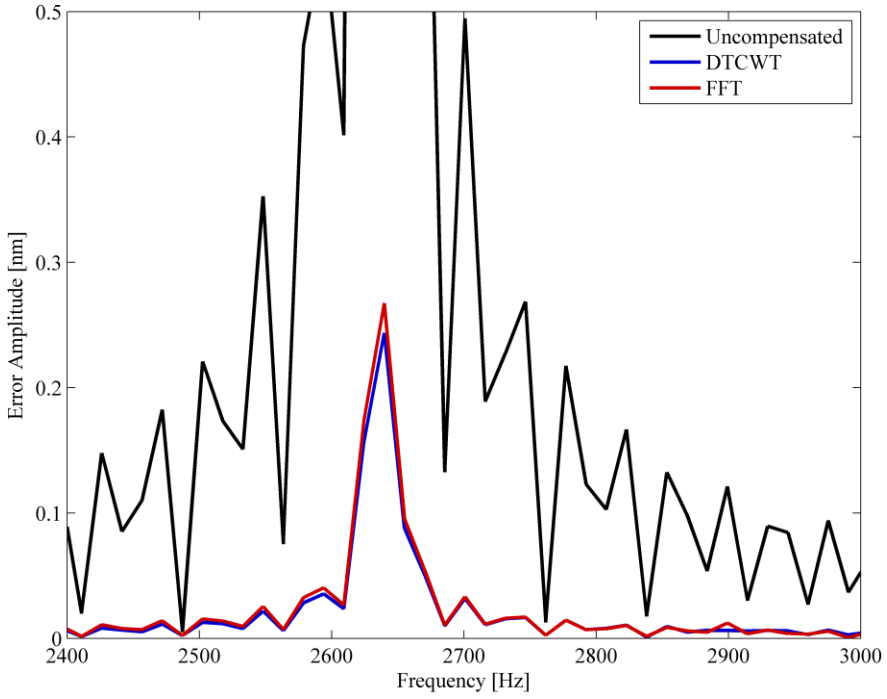


(b)

Figure 4.10 (a) The result of periodic error compensation in the frequency domain is presented. (b) Zoomed view of the compensation result for first order periodic error.

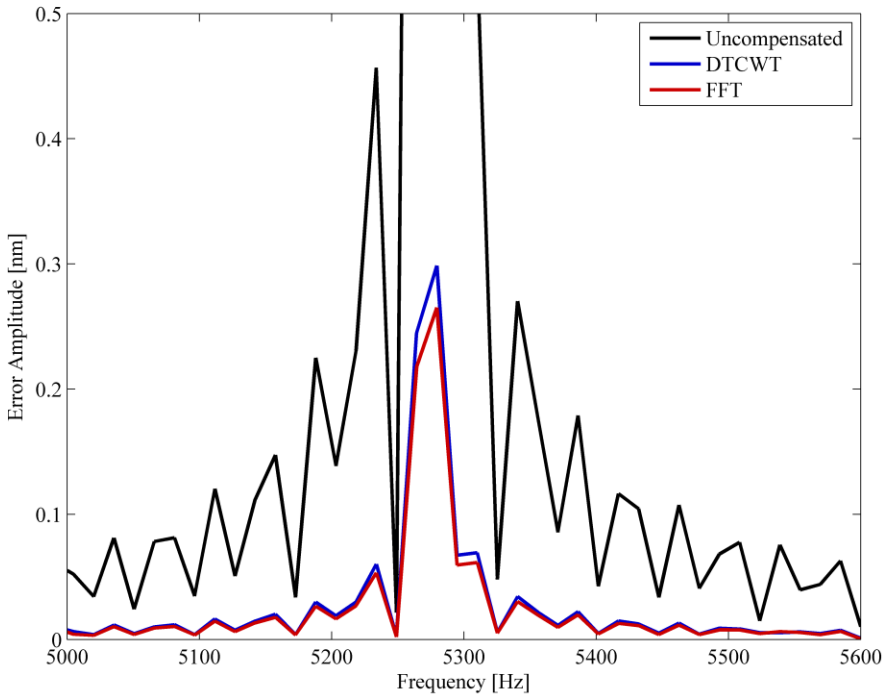


Figure 4.10 (continued) (c) Zoomed view of the compensation result for second order periodic error.

# CHAPTER 5

## CONCLUSIONS AND FUTURE WORK

This chapter includes an overall conclusion to this work, from Chapter 1 to 4, and outlines directions for future research.

### 5.1 CONCLUSIONS

This thesis introduces a novel wavelet-based periodic error measurement and compensation method that can be used to compensate periodic errors for both constant and non-constant velocity profiles in real-time.

Chapter 1 provides background of interferometry. Two types of interferometers are introduced. Error sources in heterodyne interferometry are analyzed, and the focus is on periodic error. The traditional frequency domain compensation approach for periodic error and its limitation are also given.

Chapter 2 introduces wavelet analysis, including DWT and CWT. For CWT, related equations, typical wavelets that could be used, and the linearity property are given. The complex Morlet wavelet is described in detail since it is used in the algorithm. The complex Morlet wavelet is suitable because it enables localization in both the time and frequency domains. The frequency of the periodic error signal is located at the scale with the maximum wavelet coefficient and the phase information can be extracted based on the real and imaginary parts of this coefficient.

Chapter 3 describes the entire algorithm design process. It starts from the simplified periodic error model, shows the discrete form of the CWT, and explains the edge effect and its reduction methods. The implementation of the algorithm consists of detrending the signal, applying the wavelet transform, identifying the ridge, phase and amplitude, and finally reconstructing and compensating periodic error.

Chapter 4 shows the simulation results using the wavelet-based algorithm. A linear displacement profile is used in the simulations. Identifications of ridge and amplitude, and the overall periodic error compensation result, are given. Factors which influence the compensation result are also discussed.

The performance of this approach was compared to the traditional frequency domain approach under constant velocity conditions and demonstrated accurate compensation results, showing its capability to compensate periodic error accurately.

## 5.2 FUTURE WORK

The algorithm presented in this work is designed to be executed on parallel hardware offering the potential application for real-time compensation of periodic error in heterodyne interferometers. In the future, the algorithm will be transplanted on the hardware, for instance, an FPGA board, to collect data and compensate the periodic error within the displacement.

Another investigation direction will be on high order periodic error compensation and compensation of periodic error with varying amplitudes at different orders.

# REFERENCES

[1] Bobroff N. Residual errors in laser interferometry from air turbulence and nonlinearity. Applied optics 1987;26(13):2676-82.

[2] Bobroff N. Recent advances in displacement measuring interferometry. Measurement Science and Technology 1993;4(9):907.

[3] Estler W. High-accuracy displacement interferometry refin air. Applied optics 1985;24(6):808-15.

[4] Schmitz T, Evans C, Davies A, Estler WT. Displacement uncertainty in interferometric radius measurements. CIRP Annals-Manufacturing Technology 2002;51(1):451-4.

[5] Schmitz T, Kim HS. Monte Carlo evaluation of periodic error uncertainty. Precision engineering 2007;31(3):251-9.

[6] Patterson S, Beckwith J. Reduction of systematic errors in heterodyne interferometric displacement measurement. In: Proceedings of the 8th International Precision Engineering Seminar (IPES). 1995. p. 101-4.

[7] Badami V, Patterson S. A frequency domain method for the measurement of nonlinearity in heterodyne interferometry. Precision engineering 2000;24(1):41-9.

[8] Badami V, Patterson S. Investigation of nonlinearity in high-accuracy heterodyne laser interferometry. In: Proceedings of the 12th annual American Society for Precision Engineering (ASPE) conference. 1997. p. 153-6.

[9] Daubechies I. The wavelet transform, time-frequency localization and signal analysis. IEEE Transactions on Information Theory 1990;36(5):961-1005.

[10] Pedrotti F, Pedrotti M, Pedrotti L. Introduction to Optics 3rd edition. New Jersey: Prentice Education; 2007.

[11] Peggs G, Yacoot A. A review of recent work in sub-nanometre displacement measurement using optical and X–ray interferometry. Philosophical Transactions of the Royal Society of London A: Mathematical, Physical and Engineering Sciences 2002;360(1794):953-68.

[12] Agilent Technologies. Achieving maximum accuracy and repeatability. Santa Clara, CA 2001.

[13] Wang C, Ellis JD. Dynamic Doppler Frequency Shift Errors: Measurement, Characterization, and Compensation. Ieee Transactions on Instrumentation and Measurement 2015;64(7):1994-2004.

[14] Schmitz T, Beckwith J. An investigation of two unexplored periodic error sources in differential-path interferometry. Precision engineering 2003;27(3):311-22.

[15] Kim H, Schmitz T, Beckwith J. Periodic error in heterodyne interferometry: Examination and Elimination. In: Halsey D, Raynor W, ed, editors. Handbook of Interferometers: Research, Technology and Applications. Hauppauge, NY: Nova Science; 2009.

[16] Schmitz TL, Houck L, Chu D, Kalem L. Bench-top setup for validation of real time, digital periodic error correction. Precision engineering 2006;30(3):306-13.

[17] Fedotova G. Analysis of the measurement error of the parameters of mechanical vibrations. Measurement Techniques 1980;23(7):577-80.

[18] Quenelle R. Nonlinearity in interferometric measurements. Hewlett-Packard Journal 1983;34(4):10.

[19] Sutton C. Nonlinearity in length measurements using heterodyne laser Michelson interferometry. Journal of Physics E: Scientific Instrumentation 1987;20:1290-2.

[20] Steinmetz C. Sub-micron position measurement and control on precision machine tools with laser interferometry. Precision engineering 1990;12(1):12-24.

[21] Oldham N, Kramar J, Hetrick P, Teague E. Electronic limitations in phase meters for heterodyne interferometry. Precision engineering 1993;15(3):173-9.

[22] Demarest FC. High-resolution, high-speed, low data age uncertainty, heterodyne displacement measuring interferometer electronics. Measurement Science and Technology 1998;9(7):1024.

[23] Edlén B. The refractive index of air. Metrologia 1966;2(2):71.

[24] Popela B. The Influence of the Atmosphere on the Wavelength of the He-Ne Laser and the Solution of Corrections of the Laser Interferometer. Journal of modern optics 1972;19(7):605-12.

[25] Jones FE. Simplified equation for calculating the refractivity of air. Applied optics 1980;19(24):4129-30.

[26] Jones FE. The refractivity of air. Journal of Research 1981;86:27-32.

[27] Schellekens P, Wilkening G, Reinboth F, Downs M, Birch K, Spronck J. Measurements of the refractive index of air using interference refractometers. Metrologia 1986;22(4):279.

[28] Birch K, Reinboth F, Ward R, Wilkening G. The effect of variations in the refractive index of industrial air upon the uncertainty of precision length measurement. Metrologia 1993;30(1):7.

[29] Číp O, Petrů F, Matoušek V, Lazar J. Direct measurement of index of refraction of air by means of high-resolution laser interferometry. Physica Scripta 2005;2005(T118):48.

[30] Cosijns S, Haitjema H, Schellekens P. Modeling and verifying non-linearities in heterodyne displacement interferometry. Precision engineering 2002;26(4):448-55.

[31] Rosenbluth A, Bobroff N. Optical sources of non-linearity in heterodyne interferometers. Precision engineering 1990;12(1):7-11.

[32] Augustyn W, Davis P. An analysis of polarization mixing errors in distance measuring interferometers. Journal of Vacuum Science & Technology B 1990;8(6):2032-6.

[33] Xie Y, Wu Y-z. Zeeman laser interferometer errors for high-precision measurements. Applied optics 1992;31(7):881-4.

[34] De Freitas J, Player M. Importance of rotational beam alignment in the generation of second harmonic errors in laser heterodyne interferometry. Measurement Science and Technology 1993;4(10):1173.

[35] Hou W, Zhao X. Drift of nonlinearity in the heterodyne interferometer. Precision engineering 1994;16(1):25-35.

[36] De Freitas J, Player M. Polarization effects in heterodyne interferometry. Journal of modern optics 1995;42(9):1875-99.

[37] Howard L, Stone J. Computer modeling of heterodyne interferometer errors. Precision engineering 1995;12(1):143-6.

[38] Wu C-m, Su C-s. Nonlinearity in measurements of length by optical interferometry. Measurement Science and Technology 1996;7(1):62.

[39] Park B, Eom T, Chung M. Polarization properties of cube-corner retroreflectors and their effects on signal strength and nonlinearity in heterodyne interferometers. Applied optics 1996;35(22):4372-80.

[40] De Freitas JM. Analysis of laser source birefringence and dichroism on nonlinearity in heterodyne interferometry. Measurement Science and Technology 1997;8(11):1356.

[41] Li B, Liang J-w. Effects of polarization mixing on the dual-wavelength heterodyne interferometer. Applied optics 1997;36(16):3668-72.

[42] Wu C-M, Deslattes RD. Analytical modeling of the periodic nonlinearity in heterodyne interferometry. Applied optics 1998;37(28):6696-700.

[43] Petrů F, Číp O. Problems regarding linearity of data of a laser interferometer with a single-frequency laser. Precision engineering 1999;23(1):39-50.

[44] Dubovitsky S, Lay OP, Seidel DJ. Elimination of heterodyne interferometer nonlinearity by carrier phase modulation. Optics letters 2002;27(8):619-21.

[45] Zhao H, Zhang G. Nonlinear error by orientation and elliptic polarization in a two-beam interferometer. Optical Engineering 2002;41(12):3204-8.

[46] Hou W. Subdivision of Nonlinearity in Heterodyne Interferometers. Fringe 2005: Springer; 2006. p. 327-33.

[47] Hou W. Optical parts and the nonlinearity in heterodyne interferometers. Precision engineering 2006;30(3):337-46.

[48] Stone JA, Howard LP. A simple technique for observing periodic nonlinearities in Michelson interferometers. Precision engineering 1998;22(4):220-32.

[49] Yin C, Dai G, Chao Z, Xu Y, Xu J. Determining the residual nonlinearity of a high-precision heterodyne interferometer. Optical Engineering 1999;38(8):1361-5.

[50] Loner D, Knarren B, Cosijns S, Haitjema H, Schallakans P. Laser polarization state measurement in heterodyne interferometry. CIRP Annals-Manufacturing Technology 2003;52(1):439-42.

[51] Knarren BA, Cosijns SJ, Haitjema H, Schellekens PH. Fiber characterization for application in heterodyne laser interferometry with nanometer uncertainty, part I: polarization state measurements. Optical Engineering 2005;44(2):025002--9.

[52] Knarren BA, Cosijns SJ, Haitjema H, Schellekens PH. Fiber characterization for application in heterodyne laser interferometry, part II: modeling and analysis. Optical Engineering 2005;44(2):025003--9.

[53] Topcu S, Chassagne L, Alayli Y, Juncar P. Improving the accuracy of homodyne Michelson interferometers using polarisation state measurement techniques. Optics communications 2005;247(1):133-9.

[54] Kim HS, Schmitz TL. Periodic error calculation from spectrum analyzer data. Precision engineering 2010;34(2):218-30.

[55] Ganguly V, Kim NH, Kim HS, Schmitz T. Sensitivity analysis of periodic errors in heterodyne interferometry. Measurement Science and Technology 2011;22(3):035305.

[56] Eom T, Kim J, Jeong K. The dynamic compensation of nonlinearity in a homodyne laser interferometer. Measurement Science and Technology 2001;12(10):1734.

[57] Tanaka M, Yamagami T, Nakayama K. Linear interpolation of periodic error in a heterodyne laser interferometer at subnanometer levels [dimension measurement]. Ieee Transactions on Instrumentation and Measurement 1989;38(2):552-4.

[58] Hou W, Wilkening G. Investigation and compensation of the non-linearity of heterodyne interferometers. Precision engineering 1992;14(2):91-8.

[59] Wu C-m, Su C-s, Peng G-S. Correction of nonlinearity in one-frequency optical interferometry. Measurement Science and Technology 1996;7(4):520.

[60] Wu C-m, Lawall J, Deslattes RD. Heterodyne interferometer with subatomic periodic nonlinearity. Applied optics 1999;38(19):4089-94.

[61] Nakatani N. Heterodyne interferometers using orthogonally polarized and two-frequency shifted light sources with super-high extinction ratio. Optical Review 1999;6(5):443-8.

[62] Lawall J, Kessler E. Michelson interferometry with 10 pm accuracy. Review of Scientific Instruments 2000;71(7):2669-76.

[63] Guo J, Zhang Y, Shen S. Compensation of nonlinearity in a new optical heterodyne interferometer with doubled measurement resolution. Optics communications 2000;184(1):49-55.

[64] Wang C, Augousti A, Mason J. Real time evaluation and correction of nonlinear errors in single frequency interferometers. Transactions of the Institute of Measurement and Control 2000;22(5):405-12.

[65] Schmitz T, Beckwith J. Acousto-optic displacement-measuring interferometer: a new heterodyne interferometer with Ångstrom-level periodic error. Journal of modern optics 2002;49(13):2105-14.

[66] Wu C-M, Lin S-T, Fu J. Heterodyne interferometer with two spatial-separated polarization beams for nanometrology. Optical and quantum electronics 2002;34(12):1267-76.

[67] Eom T, Choi T, Lee K, Choi H, Lee S. A simple method for the compensation of the nonlinearity in the heterodyne interferometer. Measurement Science and Technology 2002;13(2):222-5.

[68] Yeh H-C, Ni W-T, Pan S-S. Real-time motion control with subnanometer heterodyne interferometry. International Journal of Modern Physics D 2002;11(07):1087-99.

[69] Halverson PG, Spero RE. Signal processing and testing of displacement metrology gauges with picometre-scale cyclic nonlinearity. Journal of Optics A: Pure and Applied Optics 2002;4(6):S304.

[70] Bitou Y. Polarization mixing error reduction in a two-beam interferometer. Optical Review 2002;9(5):227-9.

[71] Lay OP, Dubovitsky S. Polarization compensation: a passive approach to a reducing heterodyne interferometer nonlinearity. Optics letters 2002;27(10):797-9.

[72] Wu C-m. Periodic nonlinearity resulting from ghost reflections in heterodyne interferometry. Optics communications 2003;215(1):17-23.

[73] Li Z, Herrmann K, Pohlenz F. A neural network approach to correcting nonlinearity in optical interferometers. Measurement Science and Technology 2003;14(3):376.

[74] Dai G, Pohlenz F, Danzebrink H-U, Hasche K, Wilkening G. Improving the performance of interferometers in metrological scanning probe microscopes. Measurement Science and Technology 2004;15(2):444.

[75] Keem T, Gonda S, Misumi I, Huang Q, Kurosawa T. Removing nonlinearity of a homodyne interferometer by adjusting the gains of its quadrature detector systems. Applied optics 2004;43(12):2443-8.

[76] Keem T, Gonda S, Misumi I, Huang Q, Kurosawa T. Simple, real-time method for removing the cyclic error of a homodyne interferometer with a quadrature detector system. Applied optics 2005;44(17):3492-8.

[77] Schmitz T, Chu D, Houck III L. First-order periodic error correction: validation for constant and non-constant velocities with variable error magnitudes. Measurement Science and Technology 2006;17(12):3195.

[78] Hong M, Jeon J, Park K, You K. Adaptive nonlinearity compensation of heterodyne laser interferometer. In: Knowledge-Based Intelligent Information and Engineering Systems. 2006. p. 545-52.

[79] Buchta Z, Lazar J. Small displacement measurements with subatomic resolution by beat frequency measurements. Measurement Science and Technology 2007;18(7):2005.

[80] Olyaee S, Nejad MS. Nonlinearity and frequency-path modelling of three-longitudinal-mode nanometric displacement measurement system. Optoelectronics, IET 2007;1(5):211-20.

[81] Teng H-K, Lang K-C. Heterodyne interferometer for displacement measurement with amplitude quadrature and noise suppression. Optics communications 2007;280(1):16-22.

[82] Schmitz T, Chu DC, Kim HS. First and second order periodic error measurement for non-constant velocity motions. Precision engineering 2009;33(4):353-61.

[83] Schluchter C, Ganguly V, Chu D, Schmitz TL. Low velocity compensation for first order periodic error caused by beam shear. Precision engineering 2011;35(2):241-7.

[84] Schmitz T, Adhia C, Kim HS. Periodic error quantification for non-constant velocity motion. Precision engineering 2012;36(1):153-7.

[85] Ellis JD, Baas M, Joo K-N, Spronck JW. Theoretical analysis of errors in correction algorithms for periodic nonlinearity in displacement measuring interferometers. Precision engineering 2012;36(2):261-9.

[86] Wu C, Su C, Peng G, Huang Y. Polarimetric, nonlinearity-free, homodyne interferometer for vibration measurement. Metrologia 1996;33(6):533.

[87] Köning R, Dixson R, Fu J, Vorburger T. The role of periodic interferometer errors in the calibration of capacitance displacement sensors for nanometrology applications. Measurement Science and Technology 2001;12(11):2002.

[88] Wu C-m. Heterodyne interferometric system with subnanometer accuracy for measurement of straightness. Applied optics 2004;43(19):3812-6.

[89] Evans C, Holmes M, Demarest F, Newton D, Stein A. Metrology and calibration of a long travel stage. CIRP Annals-Manufacturing Technology 2005;54(1):495-8.

[90] Deng Y-l, Li X-j, Wu Y-b, Hu J-g, Yao J-q. Analysis of frequency mixing error on heterodyne interferometric ellipsometry. Measurement Science and Technology 2007;18(11):3339.

[91] Daubechies I. Orthonormal bases of compactly supported wavelets. Communications on pure and applied mathematics 1988;41(7):909-96.

[92] Daubechies I. Ten lectures on wavelets: SIAM; 1992.

[93] Combes J, Grossmann A, Tchamitchian P, Pierce AD. Wavelets: Time-frequency methods and phase space. The Journal of the Acoustical Society of America 1991;89(5):2477-8.

[94] Rioul O, Vetterli M. Wavelets and signal processing. IEEE signal processing magazine 1991;8(LCAV-ARTICLE-1991-005):14-38.

[95] Meyer Y. Wavelets and applications: Paris [etc.]: Masson; Berlin [etc.]: Springer-Verlag; 1992.

[96] Ruskai MB, Beylkin G, Coifman R. Wavelets and their Applications. Jones and Bartlett Books in Mathematics, Boston: Jones and Bartlett, 1992, edited by Ruskai, Mary B; Beylkin, Gregory; Coifman, Ronald 1992;1.

[97] Donoho DL. Unconditional bases are optimal bases for data compression and for statistical estimation. Applied and computational harmonic analysis 1993;1(1):100-15.

[98] Burke B. The mathematical Microscope: waves, wavelets and beyond. A Positron Named Priscilla, Scientific Discovery at the Frontier 1994:196-235.

[99] Hubbard BB. The World According the Wavelet: The Story of a Mathematical Technique in the Making. Ak Peters 1996:227-9.

[100] Donoho DL. Nonlinear wavelet methods for recovery of signals, densities, and spectra from indirect and noisy data. In: Proceedings of symposia in Applied Mathematics. 1993. p. 173-205.

[101] Donoho DL. De-noising by soft-thresholding. Information Theory, IEEE Transactions on 1995;41(3):613-27.

[102] Saito N. Simultaneous noise suppression and signal compression using a library of orthonormal bases and the minimum-description-length criterion. In: SPIE's International Symposium on Optical Engineering and Photonics in Aerospace Sensing. 1994. p. 224-35.

[103] Wei D, Tian J, Wells Jr RO, Burrus CS. A new class of biorthogonal wavelet systems for image transform coding. Image Processing, IEEE Transactions on 1998;7(7):1000-13.

[104] Guo H. Wavelets for approximate Fourier Transformand data compression: PhD thesis, Rice University; 1997.

[105] Farge M. Wavelet transforms and their applications to turbulence. Annual Review of Fluid Mechanics 1992;24(1):395-458.

[106] Haar A. Zur theorie der orthogonalen funktionensysteme. Mathematische Annalen 1910;69(3):331-71.

[107] Szu H, Hsu C, Sa LD, Li W. Hermitian Hat wavelet design for singularity detection in the PARAGUAY river level data analysis. Proceeding of SPIE The International Socity for Optical Engineering 1997;3078:96-115.

[108] Ormsby RRH, Klauder B. A choice of wavelets. CSEG Recorder 1994;19:8-9.

[109] Taner M. Joint Time/Frequency Analysis, Q Quality Factor and Dispersion Computation Using Gabor-Morlet Wavelets or the Gabor-Morlet Transform. RSI Technical Report. 2001.

[110] Liu H, Cartwright AN, Basaran C. Moire interferogram phase extraction: a ridge detection algorithm for continuous wavelet transforms. Applied optics 2004;43(4):850-7.

[111] Cherbuliez M, Jacquot P. Phase computation through wavelet analysis: yesterday and nowadays. Fringe. 2001. p. 154-62.